Diurnal to Seasonal Dynamics of Groundwater, Evaporation, and Hydrology Fluctuations at the Bonneville Salt Flats Saline Pan

Jeremiah Amen Bernau[1], Brenda Bowen[1], Eric R Pardyjak[1], and Evan L Kipnis[2]

[1]University of Utah
[2]University of Utah Geology and Geophysics

November 24, 2022

Abstract

Saline pans are environments with evaporite crusts, high-salinity surface and groundwater brines, and low topographic gradients. These characteristics make them sensitive to diverse hydrological processes. The Bonneville Salt Flats, a valued and changing saline pan, was investigated to identify saline pan hydrology responses to diurnal to seasonal cycles. Seasonal changes in evaporation and relationships between groundwater levels and environmental processes in saline pans are not well understood. The results presented here, which improve characterizations of saline pan water balances and movement, enable predictions of salt growth or dissolution associated with geoengineering to mitigate the impacts of mining saline pans. Three months of eddy-covariance evaporation measurements were collected, spanning a flooded to desiccated surface transition. Two techniques, an artificial neural network and an albedo-based calibration of the Penman equation, were evaluated and used to estimate evaporation with over four years of inexpensive micrometeorological measurements. Albedo, a water availability proxy, inversely correlated with evaporation. Shallow groundwater levels varied seasonally by >50 cm and daily by >6 cm in response to temperature fluctuations. Groundwater level fluctuations should be carefully interpreted as they may not reflect recharge or discharge. Evaporation had a minor, <10 cm y-1, effect on groundwater levels. Surface moisture, primarily from rain, controlled evaporation. Summer desiccated surface evaporation was ˜0.1 mm d-1. The net annual water balance was < +/-1.5 cm y-1, indicating the saline pan stabilizes the water table. Surface dynamics of these environmentally-sensitive and variable landscapes are increasingly important to understand as water scarcity in arid environments rises.

Diurnal to Seasonal Dynamics of Groundwater, Evaporation, and Hydrology Fluctuations at the Bonneville Salt Flats Saline Pan

J. A. Bernau[1], B. B. Bowen[1,2], E. R. Pardyjak[3], and E. L. Kipnis[1]

[1]Geology and Geophysics, University of Utah, Salt Lake City, UT, USA; [2]Global Change and Sustainability Center, University of Utah, Salt Lake City, UT, USA; [3]Mechanical Engineering, University of Utah, Salt Lake City, UT, USA

Corresponding author: Jeremiah Bernau (jeremiahbernau@gmail.com)

Key Points:

- Over four years of evaporation were estimated by using eddy-covariance measurements to calibrate micrometeorological measurements.
- Saline pan albedo, which reflects water availability, can be used to calibrate evaporation estimates.
- Seasonal to diurnal temperature fluctuations have significant impacts on groundwater levels.

Abstract

Saline pans are environments with evaporite crusts, high-salinity surface and groundwater brines, and low topographic gradients. These characteristics make them sensitive to diverse hydrological processes. The Bonneville Salt Flats, a valued and changing saline pan, was investigated to identify saline pan hydrology responses to diurnal to seasonal cycles. Seasonal changes in evaporation and relationships between groundwater levels and environmental processes in saline pans are not well understood. The results presented here, which improve characterizations of saline pan water balances and movement, enable predictions of salt growth or dissolution associated with geoengineering to mitigate the impacts of mining saline pans. Three months of eddy-covariance evaporation measurements were collected, spanning a flooded to desiccated surface transition. Two techniques, an artificial neural network and an albedo-based calibration of the Penman equation, were evaluated and used to estimate evaporation with over four years of inexpensive micrometeorological measurements. Albedo, a water availability proxy, inversely correlated with evaporation. Shallow groundwater levels varied seasonally by >50 cm and daily by >6 cm in response to temperature fluctuations. Groundwater level fluctuations should be carefully interpreted as they may not reflect recharge or discharge. Evaporation had a minor, <10 cm y^{-1}, effect on groundwater levels. Surface moisture, primarily from rain, controlled evaporation. Summer desiccated surface evaporation was ~0.1 mm d^{-1}. The net annual water balance was < ±1.5 cm y^{-1}, indicating the saline pan stabilizes the water table. Surface dynamics of these environmentally-sensitive and variable landscapes are increasingly important to understand as water scarcity in arid environments rises.

Plain Language Summary

Saline pans are vast, awe-inspiring, salt-encrusted landscapes that form from the evaporation of saline water. We describe four years of observations, including measured evaporation and groundwater levels at the Bonneville Salt Flats saline pan. We examine how water moves through this system over time. We tested inexpensive methods of estimating evaporation and used these methods to study water balances. We found that the majority of water table changes reflected temperature changes, not evaporation. Most evaporation at the saline pan center was of rainwater. The salt crust acted as a barrier to evaporation of shallow groundwater. These processes are important to understand as these environments are changed by increasing desertification. The Bonneville Salt Flats saline pan formed when there was more regional water and solute input into the saline pan and evaporation significantly exceeded precipitation; this differs from current conditions. Additionally, seasonal fluctuations in groundwater levels in these systems do not reflect regional changes in discharge and recharge.

1. Introduction

Saline pans are dynamic environments where hydrology, mineralogy, and landscape evolution are strongly coupled (Rosen, 1994; Tyler et al., 2006). Evaporite-containing basins have become increasingly important in the past century as desertification has increased and lithium and potassium extraction and anthropogenic water use have led to the global decline of saline lakes and pans. These changes can inadvertently increase sources of aerosolized dust and impact air quality and human health (e.g. the Salton Sea and the Salar de Atacama) (Boutt et al., 2016; Kipnis & Bowen, 2018; Marazuela et al., 2019b; Wurtsbaugh et al., 2017). Saline pan environmental fluxes and surface properties change as they oscillate between flooding and desiccation periods (Craft & Horel, 2019; Nield et al., 2015). The mechanisms that control evaporation and hydrology within saline pans and how these processes change over time are not fully understood. Environmental measurements can improve understanding of the mechanisms and feedbacks between climate, hydrology, and the evolution of saline pans. This study uses a suite of hydrological and meteorological measurements to observe feedbacks between the halite crust, evaporation, and groundwater fluxes over four years at the Bonneville Salt Flats.

Hydrology is integral to understanding and interpreting saline pans (Rosen, 1994). These systems form when saline minerals crystallize as surface water and groundwater evaporate. Groundwaters in and around saline playas often represent regional flow paths' terminus (Lerback et al., 2019; Rosen, 1994). Delineation of evaporation rates helps constrain long-term solute and hydrological budgets and informs understanding of saline pan formation and alteration (Garcia et al., 2015; Mason & Kipp, 1998). Improved knowledge of saline pan sediments and processes can inform astrobiology, sedimentology, paleoclimatology, and evaporite-related resource management (Lowenstein et al., 1989). Since saline pan waters can remain liquid across a wider range of environmental conditions than fresh water environments and host and preserve microbial ecosystems, saline pans are increasingly studied as Martian analogs (Benison & Bowen, 2006; Benison & Karmanocky, 2014). Evaporite mineral formation and alteration rates are directly influenced by hydrology and evaporation rates. Both regional micrometeorology and understanding of climatic trends can be improved by studying and describing saline pans, which can be very extensive (>1000 km^2) (Craft & Horel, 2019; Kampf et al., 2005; Tyler et al., 2006).

Highly saline shallow or intermediate waters underlie approximately 16% of the earth's land area (van Weert & van der Gun, 2012). Saline pan hydrology differs from other, more humid settings in response to changes in evaporative demand, temperature, and regional recharge (Tyler et al., 2006). Large diurnal water-level fluctuations have been observed in these systems (Turk, 1975). High-salinity brines create gradients that can lead to density-driven groundwater convection (Van Dam et al., 2009; Duffy & Al-Hassan, 1988; Fan et al., 1997; Wooding et al., 1997). Differences in hydraulic conductivity and density between saline pans and regional groundwater flow prevent groundwaters from mixing. Fresher regional groundwater flows along alluvial fans and discharges at the surface around the edges of saline pans (DeMeo et al., 2003; Duffy & Al-Hassan, 1988; Fan et al., 1997; Garcia et al., 2015; Huntington et al., 2014; Munk et al., 2021). Although these landscapes are characterized by the remnants of evaporation (evaporites), evaporation rates are minimal despite groundwater within cm of the surface (Kampf & Tyler, 2006). Low evaporation rates and numerical groundwater flow modeling of playas, including saline pans, indicate that modern saline pans contribute to <2% of a basin's groundwater discharge in the western United States (Jackson et al., 2018). This highlights saline pans' ability to stabilize groundwater levels and associated landscape surfaces.

This work aims to use the Bonneville Salt Flats to investigate how saline pan hydrology, specifically evaporation and groundwater levels, responds to processes occurring at daily to seasonal time scales. Techniques to use long-term, inexpensive meteorological equipment measurements to estimate saline pan evaporation rates are presented and evaluated. These results and methods can help constrain environmental processes, coupling, and response rates to environmental changes within other saline pans. This robust dataset is used to examine mechanisms and controls upon saline pan water fluxes and water levels. Furthermore, hydrological budgets can use these methods to improve understanding of the role and mechanisms of groundwater evaporation upon evaporite development, resource evolution, and landscape change.

2. Background

2.1. Hydrogeological setting

This study was conducted at the Bonneville Salt Flats (BSF), Utah, on traditionally Newe/Western Shoshone and Goshute lands. BSF consists of a thin (<2 m) lens-shaped deposit of halite and gypsum that overlays laminated carbonate lacustrine sediments (Bowen, Kipnis, et al., 2018). Groundwater in this system is near or within 1 m of the surface and ranges from hypersaline (>1.2 g cm^{-3}) to saline (1.10 to ≤1.19 g cm^{-3}) (Lines, 1979). The saline pan's hydrology has been studied extensively since the 1960's (Kipnis & Bowen, 2018; Lines, 1979; Mason & Kipp, 1998; Turk, 1973). BSF's largest hydrological fluxes are evaporation and precipitation (Mason & Kipp, 1998). Surface water at BSF is sourced locally from rainfall and is distributed across its surface by wind. Mason and Kipp (1998) reported that precipitation at the edge of BSF was within 5% of precipitation at the saline pan's center, indicating that precipitation is relatively consistent across the surface (Figure S1). BSF's water table's potentiometric surface slopes away from the center of the saline pan, down to the northwest and east, limiting lateral input of groundwater at the study location at the center of BSF (Lines, 1979; Kipnis & Bowen, 2018). BSF is the drainage terminus at the northern end of a subbasin in Utah's Great Salt Lake Desert. Since 1907, infrastructure south of BSF has limited water inputs from the larger basin (Kipnis & Bowen, 2018).

Past BSF saline-pan evaporation estimates, from pan evaporation, the Bowen-ratio method, and surface halite growth rates ranged from 1.3 to 3 mm d^{-1} when the surface was flooded to 0.001 to 0.50 mm d^{-1} when the surface is desiccated (Lines, 1979; Mason & Kipp, 1998). Tyler et al. (1997) evaluated several evaporation techniques and found that only the eddy-covariance and lysimeter techniques were sensitive enough to accurately measure saline pans' low evaporation rates. Low evaporation rates from BSF's desiccated surface are comparable to other saline pans and playas, which have average evaporation rates of 0.21 mm d^{-1} (Allison & Barnes, 1985; Costelloe et al., 2011; DeMeo et al., 2003; Garcia et al., 2015; Hang et al., 2016; Jacobson & Jankowski, 1989; Kampf et al., 2005; Lines, 1979; Malek & Bingham, 1990; Mardones, 1998; Menking et al., 2000; Sanford & Wood, 2001; Schulz et al., 2015; Tyler et al., 1997; Ullman, 1985). Evaporation of groundwater from saline pans is so low that it is often within eddy covariance measurement errors of 4 cm y^{-1} (0.1 mm d^{-1}), making it challenging to quantify groundwater evaporation from saline pans (Garcia et al., 2015; Kampf et al., 2005).

BSF's surface undergoes stages where it is flooded and desiccated. Annually, there are autumn and spring periods of surface flooding at BSF (Bowen et al., 2017). Surface moisture at BSF is directly related to albedo. Decreasing albedo correlates with increasing water availability (Craft & Horel, 2019). Surface flooding is uneven over the surface of BSF. A persistent seasonal pond occurs along BSF's northwest side. Past research and Landsat 8's normalized difference water index indicate that, after the western pond, this study's location at BSF's center, is the second-most moist area on BSF's crust (Figure 1) (Bowen et al., 2017; Craft & Horel, 2019).

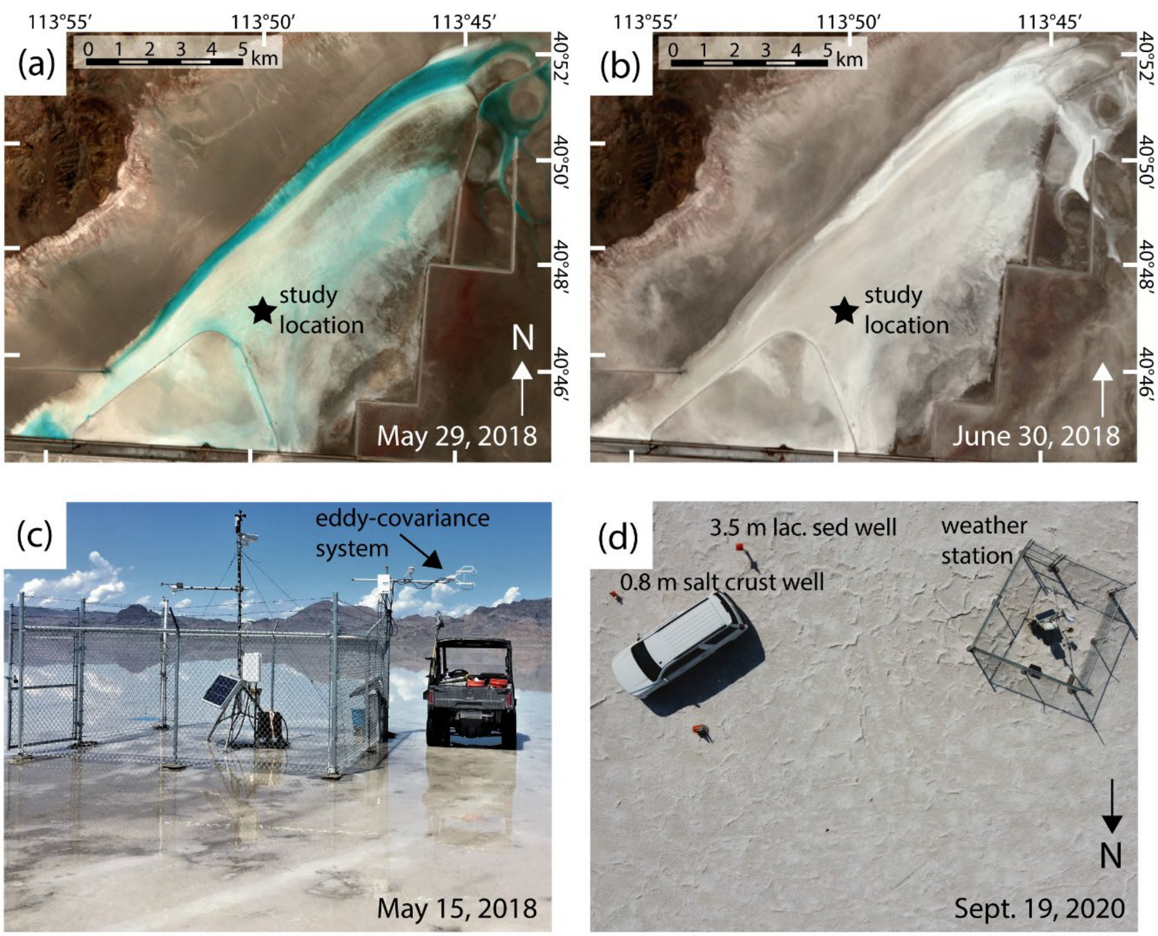

Figure 1. Overview of study location. (a-b) Contrast-enhanced false-color Landsat 8 images (bands 5, 4, and 3 as red, green, and blue, respectively), showing the presence of water (blue) during representative (a) flooding and (b) desiccation period conditions (2018). The black star indicates the study location in the middle of BSF. The linear features to the east are brine drainage ditches. The parallel lines at the base are Interstate 80. (c) Flooded surface at the weather station site at the beginning of the calibration period looking to the southwest. (d) Image of the surface of the study location weather station and wells after a sustained dry period (vehicle for scale). Date is shown on the lower right corner of each image.

Anthropogenic processes alter BSF's hydrology. Up to several billion liters of groundwater are harvested annually, leading to local decreases in groundwater level (Kipnis & Bowen, 2018; Lines, 1979). Brine created by dissolving the evaporation mine's halite by-product with brackish water from the alluvial fans of the mountains adjoining BSF to the west is introduced onto BSF in February and March through an experimental geoengineering salt restoration program. Cumulatively, more brine has been introduced into BSF than extracted through this program, which started in 1998 (Figure S2).

2.2. Mineralogy and salinity impact hydrology

Saline crusts and water salinity substantially impact radiative, thermal, and evaporative fluxes. Brines and evaporite crusts create osmotic resistance and physical impediments to groundwater vapor fluxes, thereby severely limiting evaporation(Li & Shi, 2019; Nachshon et al., 2011, 2018; Schulz et al., 2015). Water activity, the equivalent vapor pressure of the atmosphere in relation to a brine, decreases with increasing brine salinity (Calder & Neal, 1984; Mor et al., 2018; Turk, 1970). Potential evaporation decreases with lowering water activities. BSF's predominantly sodium-chloride brines have a water activity of ~0.74 (Text S2). A groundwater evaporation extinction depth for saline pans was estimated at 0.5 m at Salar de Atacama (Marazuela et al., 2019a).

Interpretation of groundwater levels requires an understanding of the factors that control water-table levels. Tyler et al. (2006) showed that water table fluctuations in response to hydrological forcings, such as precipitation and evaporation, are muted when the water-table depth is below 0.2 to 0.5 m. Temperature influences saline pans' water-table depths seasonally (Garcia et al., 2015; Turk, 1973). On shorter timescales, diurnal temperature and air-pressure changes can also influence the water-table levels by several cm and almost immediately impact water level (Turk, 1975). Temperature affects water level by altering the capillary surface tension and changing the volume of air entrapped in pores (Meyer, 1960; Turk, 1975). The impacts of surface temperature on water level decrease with increasing water depth.

3. Methods

The methods used in this study are discussed in more detail in Text S1, S2, and S3.

3.1. Eddy-covariance data

An EC 150 CO_2/H_2O open-path infrared gas analyzer (IRGA) and CSAT3 3-D sonic anemometer/thermometer open path eddy-covariance system (Campbell Scientific, Inc., Logan, UT) was installed at 2.6 m height along with an HMP45C temperature/relative humidity sensor (Vaisala, Vantaa, Finland). High-frequency IRGA and sonic data were collected at 20 Hz and slow-response temperature and humidity data at 1 Hz using a CR3000 (Campbell Scientific, Inc., Logan, UT). Data were collected near BSF's center from May to August 2018 (the calibration period, Figure 1C). Latent and sensible heat fluxes were calculated by applying the eddy-covariance technique with 30-minute averaging intervals. Standard turbulence-flux corrections and quality control measures were applied following Jensen *et al.* (2016). Data gaps in evaporation measurements determined during quality control were filled with values generated with an artificial neural network (Kang et al., 2019). This study focuses on daily sums of evaporation, so ground heat flux was not measured. Sonic anemometer data were used to calculate BSF's aerodynamic roughness (de Bruin & Holstag, 1982; Nield et al., 2013).

3.2. Weather-station data

Research-grade weather station data collected at 5-minute intervals spanned from September 27, 2016 to the Spring of 2021 (the study period). Incoming and outgoing longwave and shortwave radiation were measured with an Apogee SN-500 net radiometer (Logan, Utah, USA, installed June 6, 2017). Before June 2017, incoming and outgoing shortwave radiation were measured with LI-200R solar sensors pointing upwards and downwards (400 to 1100 nm; LI-COR, Lincoln, Nebraska). Additional sensors include a Vaisala PTB110 pressure gauge; Texas Instruments TR-525USW unheated tipping bucket rain gauge; Vaisala HMP60 air temperature and relative humidity sensor at 2 m; and a R. M. Young 05103 anemometer at 3 m. A Campbell Scientific soil temperature sensor buried at 10 cm depth and an Axis Communications web camera were also installed on June 6, 2017. Weather station data gaps were filled with regional environmental measurements, an artificial neural network, and linear extrapolation. Weather-station data averaged over 30-minute intervals was used to calculate albedo, potential evaporation adjusted for water activity (PE), and estimated evaporation using an artificial neural network (E_eANN) and an albedo-calibrated modification of the Penman-equation (E_eLow and E_eHigh).

Albedo (α) was calculated with Equation 1, where the sum of daily outgoing shortwave radiation (SW_{out}) between sunrise and sunset (dt) is divided by the sum of daily incoming shortwave radiation (SW_{in}) over the same period. Surface moisture was quantified with albedo measurements (Craft & Horel, 2019) and was confirmed using time-lapse imagery (Bernau & Bowen, 2020).

$$\alpha = \frac{\int SW_{out}\,dt}{\int SW_{in}\,dt} \quad \textbf{(1)}$$

3.3. Potential evaporation

A modified Penman equation was used to calculate potential daily evaporation corrected for water activity (Equation 2) (Calder & Neal, 1984; Malek & Bingham, 1990). Transpiration at this site is negligible because it lacks macroflora.

$$PE = \left(\frac{\Delta}{\Delta+\frac{\gamma}{\beta}}\left(R_n + H_g\right) + \frac{\gamma}{\Delta+\frac{\gamma}{\beta}}15.36(0.75 + 0.0115U_2)\left(e_s - \frac{e}{\beta}\right)\right)86400/\lambda \quad \textbf{(2)}$$

where PE is potential evaporation (mm d^{-1}); Δ is the slope of the saturation-vapor-pressure curve (kPa/°C); γ is the psychometric constant (kPa/K); β is the water activity (0.74); R_n is net radiation (W/m^2); U_2 is the wind speed at 2 m height (m/s); e_s is the saturation vapor pressure at temperature T (kPa); e is the vapor pressure (kPa); and λ is the latent heat of vaporization (J/kg) (1 kg H_2O = 1 mm H_2O/m^2). H_g is the ground heat flux, which could not be calculated with available equipment. Ground heat flux is negligible over daily timescales, and was not considered because only daily potential evaporation values were used to measure long term fluxes (Allen et al., 1998). Unless otherwise noted, PE in this work refers to PE corrected for water activity.

3.4. Estimated evaporation

Estimated evaporation (E_e) was calculated by multiplying PE by a crop coefficient (K_c) calibrated with the eddy-covariance data and a daily albedo value (Equation 3). The calibration was segmented for two albedo ranges: albedo <0.37, and albedo ≥0.37. Evaporation fell sharply and stabilized as the surface dried out, at an albedo of ≥0.37. Two models were used to create evaporation estimates when the surface was desiccated to address variability between measured and estimated evaporation (Figure S4). A dry surface Kc was multiplied by albedo in the first model (E_eHigh). A constant scaling factor was used in the second model (E_eLow).

$$E_e = K_c \frac{PE}{\alpha} \quad \textbf{(3)}$$

Implementing the methods of Kelley and Pardyjak (2019), artificial neural network models were used to estimate evaporation (E_eANN). The input 30-minute average values of the weather-station observations were trained to replicate evaporation measured by the eddy-covariance method. The effectiveness different input parameters was assessed by comparing artificial neural network model evaporation estimates to E_eHigh and E_eLow values (Figure S5). The model discussed in this work incorporates humidity, air temperature, air pressure, wind speed, shortwave radiation (net and in), longwave radiation (net and out), and time of day as inputs. Because the model outputs were not normally distributed, the median value of each 30-minute interval over 1000 models was used. The upper and lower quartile values are also shown to demonstrate the variability in model output. Variability is considered a measure of model robustness and generality (Kelley et al., 2020). Periods with larger interquartile ranges indicate higher uncertainty in artificial neural network modeled evaporation values.

Eddy covariance equipment was only installed at BSF's center from May to August 2018, making winter periods with low temperatures and high humidity outside of the artificial neural network's training dataset. To test the effect of removing these conditions from the training dataset, the artificial neural network was run with training data incrementally trimmed to remove progressively lower humidity and higher temperature periods. Modeled outputs after each increment were saved and then compared (Figure S5). When the training dataset was limited to higher temperatures, winter evaporation estimates were elevated, indicating neural network model outputs overestimate winter evaporation because they did not have cold winter temperature in their training data. To counter this, neural network model outputs greater than potential evaporation (PE) or two times greater than albedo-calibrated estimated evaporation (E_eHigh) were replaced with the neural network's 25th percentile values. If the 25^{th} percentile values exceeded these parameters, model outputs were replaced with E_eHigh values.

3.5. Groundwater-level data

Pressure-temperature transducers (U20L-04 and U20L-01, Onset, Bourne, Massachusetts, USA) were installed in a 3.5-m deep well screened in lacustrine sediments (lacustrine sediment well) between December 2017 to June 2021. Pressure-temperature transducers were installed in a 0.8-m deep well screened within the salt crust (salt crust well) from September 2019 to September 2021. Both wells were within 20 m of the weather station (Figure 1D). Additional wells dispersed across the saline pan were also considered.

The water depth in the saline salt crust well was more representative of the water table. The 3.5-m deep well was less saline. To make the water levels in the 0.8 and 3.5-m deep wells more comparable their heads were corrected by using Equation 4 (Post et al., 2007) (Figure S6).

$$h_1 = \frac{\rho_2}{\rho_1} h_2 - \frac{\rho_2 - \rho_1}{\rho_1} z \qquad \textbf{(4)}$$

where ρ_1 is the reference density to adjust the sample to (the average annual density of halite-saturated brine, 1.21 g cm^{-3}); ρ_1 is the density of the well-water; h_2 is the height of the water level above a datum (sea-level) as was measured using a depth to water meter or pressure transducer; z is the elevation (above the sea-level datum) of the mid-point of the screened interval; and h_1 is the equivalent head relative to the datum.

Water levels in the 3.5-m lacustrine sediment wells changed in response to air pressure changes, indicating it did not have high barometric efficiency. Measured changes in water level were influenced by the differential between atmospheric pressure at the well and at the aquifer (McMillan et al., 2019). The median-of-ratio's and linear regression methods over hourly and daily timescales were used to determine well's barometric efficiency (Turnadge et al., 2019). Because the effect of air pressure changes upon water level was quantified, these changes could be removed from the observed water level changes to determine what water levels would be if the wells had a perfect barometric efficiency and their water levels did not change in response to air pressure changes (Figure S7). If applying the barometric efficiency to water levels increased their variability, the calculated barometric efficiency was not used and was assumed to be one.

Similar to barometric efficiency, daily and seasonal water level fluctuations were influenced by temperature; this effect is defined here as a well's thermal efficiency. The barometric efficiency framework can be applied to calculating and applying corrections for thermal efficiency. Periods with water movement in and out of the system or water levels above the surface are removed from datasets before using them to determine a well's thermal efficiency with barometric-efficiency-corrected water level measurements. Because of lags in temperature peaks with water depth, daily ranges of water level and soil temperatures were used to calculate daily thermal efficiencies with the median-of-ratios method. Weekly to monthly intervals were used to calculate seasonal values of thermal efficiency with the median-of-ratio's method. The thermal efficiency could be used to correct water levels to understand how they would change if temperature fluctuations were not affecting levels.

The apparent specific yield was calculated with a water budget equation. The apparent specific yield was determined from the change in water level over a period given a known change in water balance (Gerla, 1992; Lv et al., 2021; Walton, 1970). The apparent specific yield was used to quantify evaporation from groundwater changes in groundwater levels corrected for barometric and thermal efficiency, and density.

4. Results

The results of evaporation estimation methods applied during the calibration period are reviewed, then the results of the full study period are described. Controls upon water level fluctuations are described. Finally, daily fluxes in evaporation and water level throughout the year are reported.

4.1. Calibration period

Evaporation rates from the surface were relatively high at the beginning of the calibration period, when the surface was flooded (Figure 1C). Evaporation sharply decreased over time, briefly increasing after rainfall (Figure 2A). Depth to groundwater reflected evaporation. Evaporation was elevated when the water level was at or within 5 cm of the surface (Figure 2A and 2C). During the desiccation stage, the average daily evaporation rate was ~0.1 mm d^{-1}. The potential evaporation rate, 2.3 mm d^{-1}, was >20 times higher than actual evaporation. The aerodynamic roughness length was similar to other playas at 5.4×10^{-4} m (Jensen et al., 2016; Marticorena et al., 2006). Evaporation was negatively correlated with albedo (Figure 2D, r^2: 0.90). Evaporation was positively related to potential evaporation divided by albedo (Figure 2E, r^2: 0.85). This relationship was used to create the albedo-calibrated estimated evaporation models (E_eHigh and E_eLow).

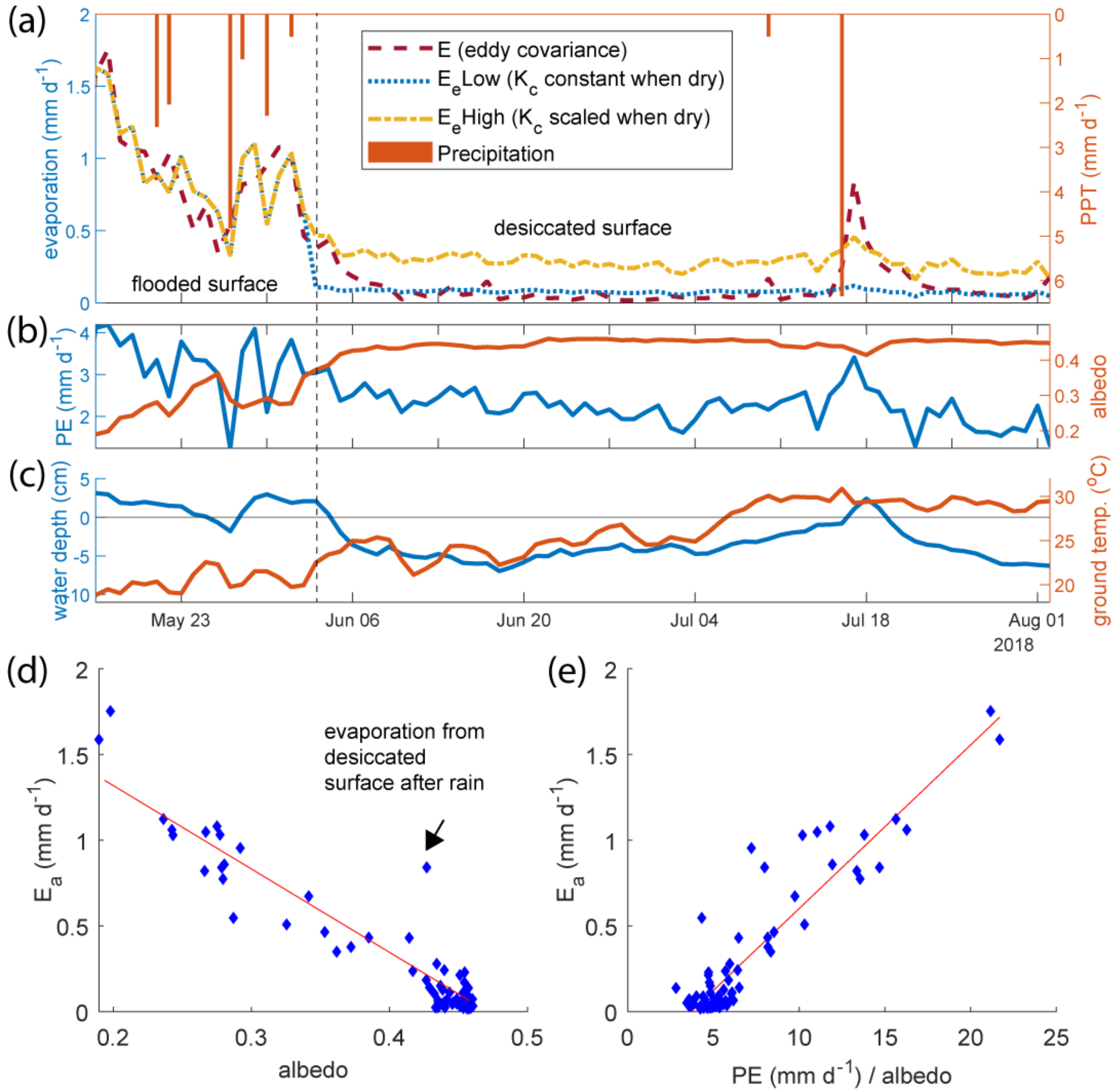

Figure 2. Environmental measurements and data relationships during the summer 2018 calibration period when the eddy-covariance system was at the Bonneville Salt Flats. (a) to (c) have the same x-axis values (a) Evaporation and precipitation (PPT). Eddy covariance evaporation was used to calibrate the albedo-adjusted evaporation estimates (E_eHigh and E_eLow). These two estimates provide bounds for evaporation during the desiccation stage. Evaporation from the artificial neural network is not shown during this period because it nearly matches evaporation values. (b) Potential evaporation (PE) is much higher than evaporation but does reflect its changes. Albedo gradually rises when the surface is flooded and plateaus during the desiccation stage. (c) Water level (adjusted for density and corrected for barometric efficiency), from 3.5 m deep well screened in lacustrine sediment, reflects changes in surface moisture indicated by albedo. Temperature is shown to highlight its impact on water levels. (d) The correlation between albedo and evaporation is robust. Evaporation after small summer rain events where the albedo does not decrease by much (July 17) is the exception to this relationship. (e) Linear correlation between evaporation and potential evaporation (PE) divided by albedo. This relationship was used to calibrate estimated evaporation (E_e) values in (a).

During the desiccation period, the relationship between evaporation and potential evaporation divided by albedo was poor (r^2: 0.05) so the two albedo-calibrated models were used to create bounds for upper (E_eHigh) and lower (E_eLow) evaporation estimates (Figure 2A). These models are dependent upon albedo, which is primarily controlled by surface moisture. However, surface buckles and dust accumulation can also decrease local albedo, artificially increasing the apparent surface moisture (Figure 1D).

Albedo stabilized during the desiccation stage, except after a 6.9 mm rain event in July 2018, which led to a minor dip in albedo and a spike in evaporation. The dip in albedo was too minor to impact the value of EeHigh significantly, but the generally elevated evaporation levels of E_eHigh compensate for this over periods greater than two weeks. This is reflected in the cumulative values of measured evaporation, E_eLow, and E_eHigh during the calibration period. E_eLow is below measured evaporation, while E_eHigh is above measured evaporation (Figure S4C). Cumulative differences between the E_eHigh and E_eLow models encompass the uncertainty of evaporation measurements during the desiccation period.

The measured daily evaporation values and the artificial neural network's estimated evaporation values were effectively the same during the calibration period. During this period, cumulative artificial neural network evaporation values were within 1% of the eddy-covariance evaporation values (Figure S4).

4.2. Full study period

4.2.1. Evaporation estimation methods

Over the full study period from Autumn 2016 to Autumn 2021 the artificial neural network's estimated evaporation (E_eANN) values were similar to evaporation estimated by the calibrated albedo-based models. In the summer months, E_eANN values were generally between the E_eLow and E_eHigh values. E_eLow values were more similar to E_eANN values than EeHigh values were, except for periods immediately following rainfall. In contrast, the corrected artificial neural network values had slightly higher evaporation estimates in winter than the other evaporation estimation models. Furthermore, E_eANN values had large interquartile ranges during winter months, indicating winter results were less robust because winter temperatures differed from the calibration periods training dataset.

4.2.2. Evaporation over time

Evaporation was highest during the wet spring months and peaked after autumn flooding (Figure 3A). Evaporation was low in the summer when the salt crust was desiccated and low in the winter when potential evaporation was minimal. There was a strong relationship between evaporation and precipitation (Figure 3). Maximum potential evaporation peaked at ~2.5-3.5 mm d^{-1}. The maximum model estimated evaporation rate was 2.5 mm d^{-1}. The length of spring flooding varied between years, but the surface consistently desiccated by July. The autumn flooding period was much smaller, and evaporation quickly decreased as the surface desiccated or as potential evaporation fell. Autumn 2020 was unusually dry, and is the only time during the study period to not have an autumn flooding period and an associated spike in evaporation.

Low albedo is generally associated with the higher estimated evaporation rates and results in increased estimated evaporation values. Time-lapse imagery shows that increases in crust roughness and dust accumulation depressed albedo. Rain dissolves surface halite and enables dust to settle. As ponded water evaporates, new, highly reflective halite crystals form, leading to high albedo values. Lower maximum albedo values during dry years (2020 and 2021), when a lack of rain impairs this process, erroneously increase evaporation estimates (Figure 3B).

Figure 4 demonstrates that the cumulative precipitation and evaporation estimates are well-aligned. The high evaporation model (E_eHigh), which overestimates evaporation, indicates evaporation exceeds precipitation annually by ~2.0 cm y^{-1} on average. The E_eANN model indicates precipitation exceeds evaporation by ~0.1 cm y^{-1} on average. Similarly, the E_eLow model indicates precipitation exceeds evaporation by ~0.7 mm y^{-1} on average. The uncorrected 25^{th} to 75^{th} ANN models indicate evaporation exceeds precipitation by -0.5 to 5.0 cm y^{-1}. Water balances vary annually. These differences are best seen with annual comparisons starting in August, which is the last month of the year to be consistently desiccated. In 2018 and 2019, BSF was water neutral to slightly water positive. All models show 2020 to have a negative water balance, 2021is similar to 2020. A negative water balance, indicating evaporation exceeds precipitation, is typically limited to spring and summer months.

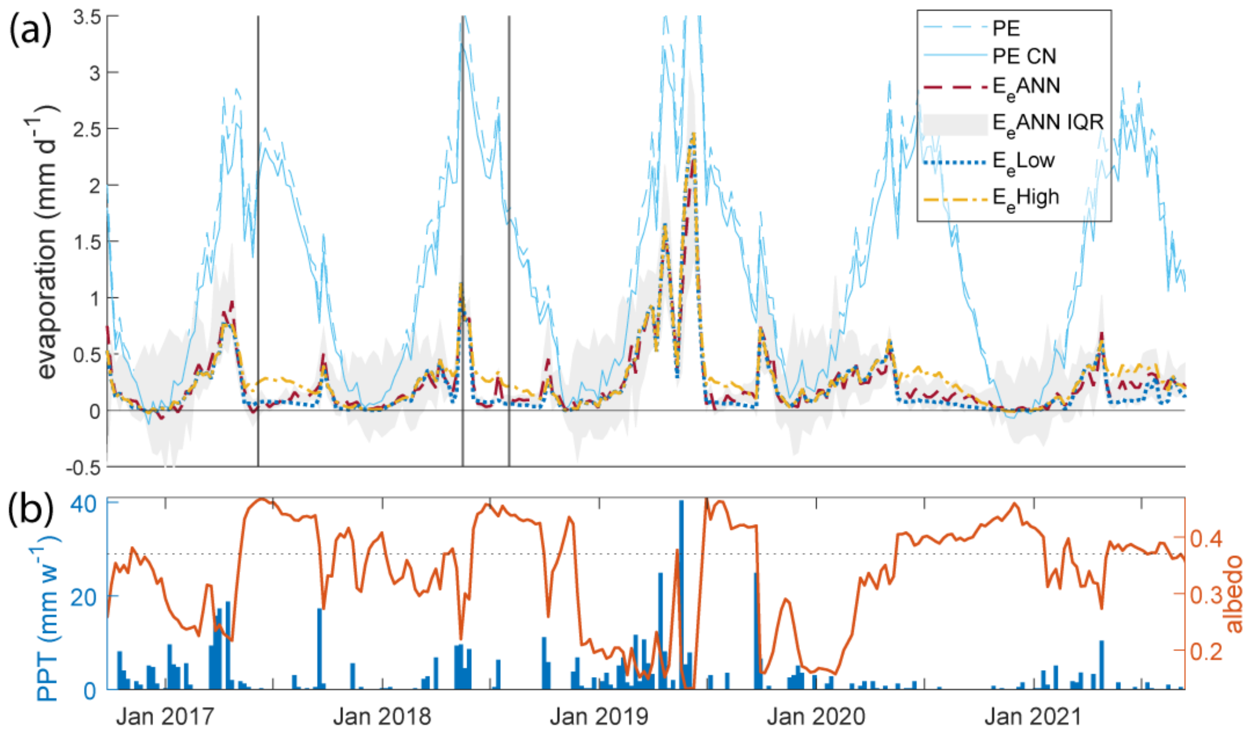

Figure 3. Weekly results of evaporation models applied to the entire dataset (Autumn 2016-Spring 2021) and associated environmental measurements. (a) and (b) have the same x-axis values. (a) Potential evaporation (PE and PE CN) far exceeded evaporation calculated with an artificial neural network and albedo-calibrated evaporation. Potential evaporation corrected for water activity (PE CN) was slightly lower (<20%) than the uncorrected potential evaporation (PE). The first vertical black line indicates when the Apogee SN-500 net radiometer and time-lapse camera were installed (June 6, 2017). Evaporation values before this period are not directly comparable to later evaporation values. The following two vertical black lines indicated the calibration period for this study (Figure 2). (b) Weekly precipitation and albedo measurements. The horizontal line indicates the cut-off value (0.37) for the albedo-calibrated evaporation models (E_eHigh and E_eLow).

4.2.3. Water balance from groundwater level

Temperature changes had a substantial impact on groundwater-level changes during dry periods. Significant decreases (<50 cm) in groundwater level occurred in dry autumns from the crust's cooling. Season thermal efficiency values were able to replicate these changes. These corrections showed that groundwater levels should have peaked in July, not May or June, indicating the effect of evaporation on summer water levels (Figure S2).

In general, groundwater evaporation rapidly decreases in the early summer as the groundwater levels declines. From May to August, ground temperatures increased ~6 °C, and groundwater levels in the 0.8 m deep well decrease by ~2 cm (~7 cm if corrected for temperature change). Of note, the average August groundwater depth in density-corrected wells at BSF's center is 10 cm (±3 cm) (Figure S8), indicating that water levels stabilize in the subsurface after two to three months of desiccation. This also makes this month ideal for year-to-year comparisons of water levels.

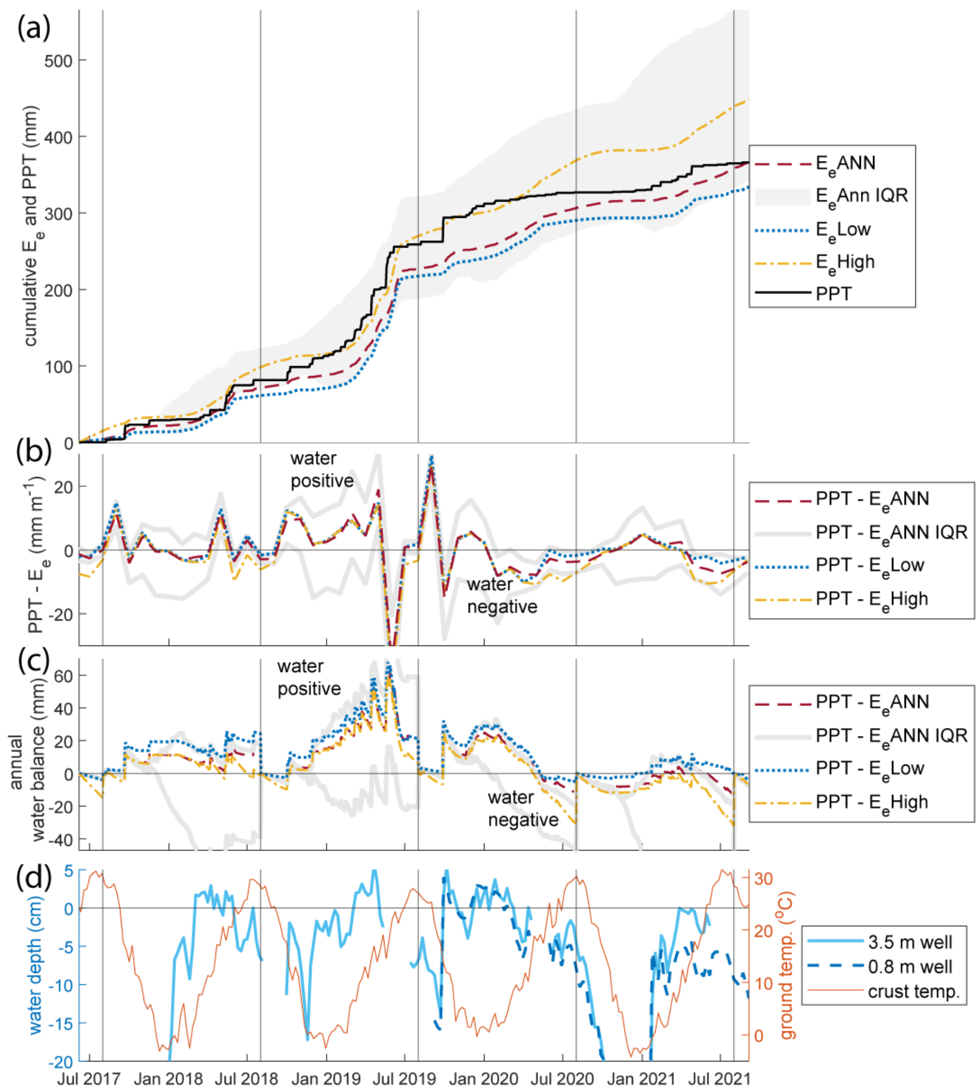

Figure 4. Measures of the water balance and water level from June 2017 to September 2021. All charts have the same x-axis values. Vertical black lines added at August 1 used to differentiate years because the water level stabilizes at roughly the same level in August each year, and the crust has been desiccated for at least one month prior to August. (a) Cumulative precipitation and estimated evaporation values. Evaporation increases after precipitation. These data indicate an annual mean net water balance (PPT - E_e) of 0.1 cm (E_eANN), 0.7 cm (E_eLow), -2.0 cm (E_eHigh). The E_eHigh model overestimates long-term evaporation. (b) Adapted Standardized Precipitation Evaporation Index (SPEI) where monthly evaporation is subtracted from monthly precipitation. Most months are water negative if potential evaporation is considered. Many water positive months were desiccated at the end of the month, e.g., November 2019, suggesting incorporation of precipitation into groundwater, overland flow of precipitation away from the system, or that evaporation was underestimated. (c) The cumulative net water balance (PPT - E_e) for each year (starting in August), 2018 and 2019 are water positive, 2020 and 2021 were water negative to water neutral for the E_eANN and E_eLow models. (d) Equivalent head water levels in the shallow salt crust (0.8 m deep) and lacustrine sediment (3.5 m deep) wells. The water level difference between the two wells shows that upward brine fluxes are buffering decreases in the saline pan water table in the summer. The water level in the wells begins to fall rapidly after August, when the air and ground temperatures decline.

The calculated apparent specific yield was 9% (standard deviation of 4%). This value likely underestimates effective specific yield over longer drainage periods with deeper groundwater levels, as the shallow crust is highly porous and permeable (average porosities of 23 to 29%). Using specific yields of 5-13%, the average change in temperature-corrected water level indicates that the normal groundwater evaporation rate from June to August is 0.06 to 0.15 mm d^{-1}, these estimates would be halved if temperature impacts on groundwater were not considered. If the majority of groundwater evaporation occurs from June to August, as inferred from changes in groundwater levels, then 0.4 to 0.9 cm y^{-1} of groundwater evaporation is occurring annually. This evaporation-rate estimate agrees with evaporation estimated with micrometeorological techniques (0.1 mm d^{-1} during the desiccation stage, and net evaporation of -0.7 to 2 cm y^{-1}).

4.3. Diurnal fluxes: daily to seasonal changes

Evaporative fluxes are very low during the desiccation stage (Figure 5). Like other saline pans (e.g. Kampf et al., 2005), it is challenging to identify diurnal patterns within evaporation measurements from a desiccated saline pan. The half-hour median values of evaporation measured with the eddy-covariance technique indicate higher evaporation occurs from sunrise to noon. There are two evening spikes in evaporation, a short one at 18:00 MST and another at 23:00 MST. Evaporation is lowest in the morning before sunrise. In contrast, diurnal evaporative fluxes during the flooding stage primarily reflected changes in potential evaporation.

Several other environmental parameters fluctuate daily during the summer desiccation stage (Figure 5). Under the atmospheric tide (Chapman & Lindzen, 1970) air pressure generally rises rapidly and peaks as evaporation with evaporation in the morning, it then falls until 20:00 MST (sunset); and then rises and stabilizes in the evening. Albedo rises after 10:00 MST. Windspeed is lowest at noon and highest in the evening, peaking at ~4 m/s at 21:00 MST.

The groundwater level in the salt crust well changes by ~6 cm from 09:00 to 18:00 MST each day. During this period, air pressure changes by the equivalent of ~3 cm of halite-saturated brine from 10:00 to 19:00 MST. Given this well's high barometric efficiency (>0.91), this change would affect water levels by <0.5 cm. The ground temperature increased by 6 °C from its minimum at 07:00 to its peak at 17:00 MST. Given this well's high summer diurnal thermal efficiency (0.76), this change would affect water levels by 4.7 cm. The thermal efficiency explains the majority of diurnal groundwater fluctuations, furthermore, the minimum and maximum water level points lag one hour behind these peaks in soil temperature, as would be suggested by a temporal lag for thermal diffusion, further support this hypothesis.

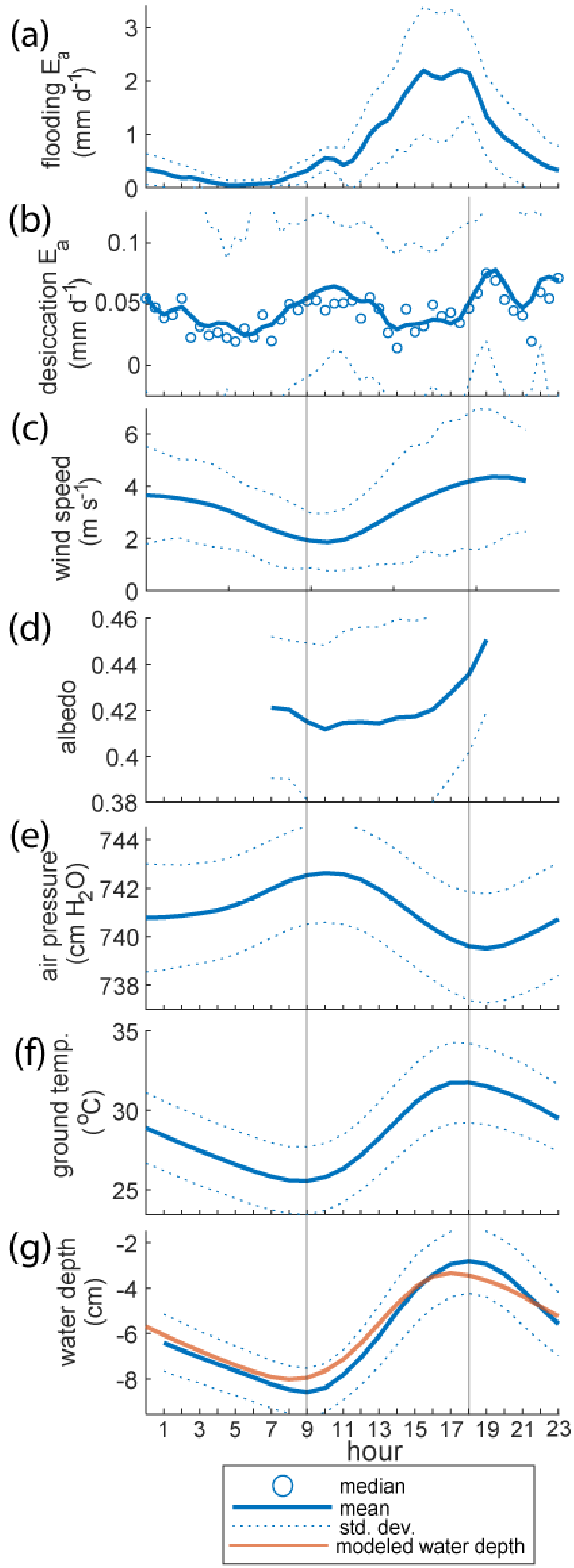

Figure 5.Diurnal fluxes over the salt crust. (a) Mean evaporation (smoothed fit) when the surface is flooded from the calibration period. (b to g) Mean fluxes when the surface is desiccated. Vertical gray lines added to highlight minimum and maximum water levels. (b) Median and mean evaporation (smoothed fit) from the desiccated surface during the calibration period. Note the peak in evaporation from the desiccated surface in the early morning (10 am) and the other peak in evaporation in the evening. (c) Wind speed is highest in the evening and lowest in the mid-morning. (d) Albedo is lowest in the early morning and rises throughout the day. (e) Air pressure (in cm of water with a density of 1.2 g cm^{-3}). (f) Ground temperature at 10 cm depth. (g) Mean water depth (from the 0.8 m salt crust well) is lowest during early morning and falls during the evening. The orange line shows the calculated water depth change due to the well's thermal efficiency, demonstrating the majority of diurnal water fluctuations are attributable to temperature fluctuations.

Seasonal trends in diurnal groundwater water-level fluctuations in the shallow salt crust well indicate that the maximum range in groundwater levels reflects seasonal temperature change (Figure 6). The well's highest diurnal thermal efficiencies occurred in summer months and daily changes in water depth were most correlated with maximum soil temperature. Groundwater levels increased sharply after rainfall and fell gradually in the subsequent weeks. Groundwater level fluctuations are highest when the water table is 4 to 8 cm below the surface on average. Diurnal temperature swings at the water table-vadose zone interface were muted by increasing groundwater depth and the insulating property of the ground in autumn to winter. Similarly, diurnal temperature variations were muted when the water table was at the surface (Figure 6B).

5. Discussion

The hydrological system at BSF is discussed here through the lens of groundwater levels, diurnal fluctuations, seasonal changes in surface water, and overall water balances. These results' implications are then discussed.

1.1. Daily to seasonal changes in groundwater level

Because evaporation rates for saline pans are so low and because their water levels can be so variable throughout the year, the controls on water-table levels must be understood if groundwater levels are used to interpret local to regional hydrological balances. Near-surface ground temperature, followed by air temperature, when scaled using a seasonal or daily thermal efficiency values predicted the majority of groundwater level fluctuations during periods with little water movement in or out of the system.

Air pressure, which mirrors temperature changes, was previously shown to influence diurnal groundwater-level fluctuations in saline pans (Macumber, 1991; Sieland, 2014; Turk, 1975). However, given the high barometric efficiency of the 0.8-m salt crust well, air pressure appears to play a minor (<10%) role in diurnal groundwater level fluctuations. Temperature changes, which were previously shown to alter the surface tension in capillary pores and the volume of pore-entrapped air (Meyer, 1960; Turk, 1975), are the primary control upon groundwater level changes when the system is water neutral.

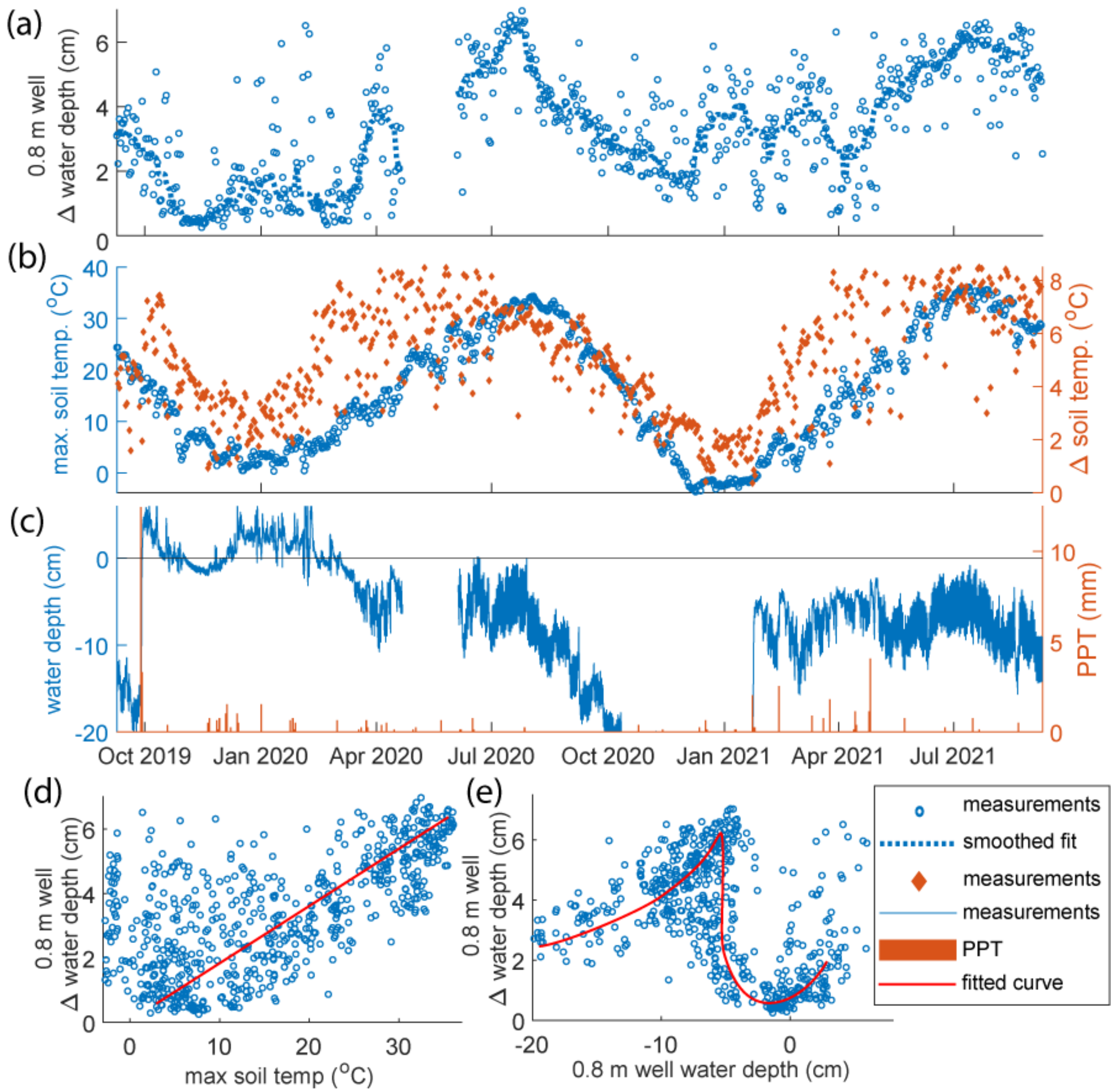

Figure 6. Daily water level changes in the 0.8 m salt crust well and associated daily environmental values. Smoothed fitted lines added to (a) to assist data interpretation. (a) Daily Δ water level ranges between ~0.5 to 7.0 cm throughout the year. Daily Δ water level are consistently high in the middle of the summer and are lower, with some days of high variation, in the autumn and winter. (b) Daily maximum 10-cm depth soil temperature and Δ soil temperature. (c) Daily precipitation and 30-minute intervals of measured water depth. Rainfall during this period was very low and contributed to a small minority of diurnal water level changes. (d) The daily Δ water depth in the 0.8 m salt crust well correlates most strongly with maximum daily soil temperature. (e) The water table depth influences daily Δ water depth. Daily Δ water level is higher when the water level is between ~4 to 8 cm below the surface.

Predicted diurnal water-level changes were slightly lower than observed groundwater water-level changes, suggesting variability in diurnal thermal efficiency. Thermal efficiency models or applications of thermal efficiency to predict groundwater levels could be improved by incorporating additional inputs and numerical modeling. For example, water levels and lags from thermal dispersion when water levels are lower could be incorporated. Seasonal and daily values of thermal efficiency differ and were uncorrelated. There is no pattern between well parameters and diurnal thermal efficiency values. Seasonal values of thermal efficiency, however, are related salt crust thickness. Wells in areas with thicker evaporites (which are more porous) being less affected by water level changes than wells in areas with little to no evaporites, which are hosted in fine grained lacustrine sediments.

Previous studies indicate that the shallow water tables in playas can rise above the surface when air pressure drops (Mason & Kipp, 1998; Turk, 1973; Tyler et al., 2006). Spontaneous water level rise above the surface from only a reduction in air pressure was not observed during this study. However, there were periods where the water table did change rapidly when the water level was near the surface with little precipitation (<2 mm). For example, time-lapse imagery and pressure transducer data in June 2021 show surface water following a minor rain event along with rapid increases in groundwater levels (6 cm rise in 30 minutes), water in a small pond rose to flood the crust surrounding it during this period. The water levels quickly returned to prior levels in the hours following this event. These observations are consistent with the Lisse effect (Heliotis & DeWitt, 1987). The Lisse effect occurs when rain traps air in the unsaturated zone, as the air volume is changed by air pressure fluctuations or as it warms and expands it displaces water, which can rise into wells, and in this case, breaks in the salt crust surface. Similar observations in other saline pans may be explained by the Lisse effect.

Estimated evaporation values indicate that the halite crust severely limits evaporation of groundwater. This research corroborates previous work that demonstrated negligible groundwater evaporation from saline pans (Jackson et al., 2018; Kampf et al., 2005). The consistent groundwater level in August at 9 cm (±2 cm) below the surface across several years indicates falling groundwater levels hinder evaporation.

Seasonal variation in groundwater levels make it challenging to interpret annual net water balances from groundwater level changes. If only spring to summer months are considered, groundwater evaporation would be 0.4 to 0.9 cm y^{-1}. This result is consistent with micrometeorological evaporation estimates. Differences between annual water balance estimates for the saline pan's center originate from uncertainties in estimating specific yield or evaporation, lateral water movement, or the eddy-covariance technique's sensitivity, which was near measurement error when the surface was desiccated.

The effect of temperature on groundwater levels should influence seasonal changes in evaporation. If winter rain decreases the water-table depth, then later temperature increases will increase groundwater levels, increasing groundwater availability for evaporation. This effect would increase spring evaporation; however, it would likely be small given annual estimated water balances (<1 cm y^{-1} evaporation increase). Bernau and Bowen (2021) previously described apparent vertical brine fluxes from differences between the 0.8 and 3.5-m well equivalent head measurements. An apparent upward gradient occurred in the summer, and a downward flux occurred in the winter. Vertical gradients originate from differences in temperature effects upon water level between salt crust and the underlying lacustrine sediment aquifer. The deeper lacustrine sediment aquifer differs from the overlying evaporite-hosted aquifer because it is shielded from temperature fluctuations, is thicker, and has much smaller pores.

At BSF's center, vertical fluxes and incorporation of rainwater into the lacustrine aquifer appears to be minor. The mean groundwater transit time measured with carbon-14 from the 3.5-m lacustrine sediment well was 10-15 thousand years old (Lerback et al., 2019). However, the same study identified modern tritium in samples, indicating some vertical mixing and integration of rainwater. In general, rainwater integration into the subsurface at BSF's center appears to be limited. This interpretation is supported by most tritium measurements that were made on BSF groundwater samples collected from 1992 to 1993, where wells at the center of BSF, with consistently high water levels, had lower tritium concentrations than wells at the edge of BSF (Mason et al., 1995).

5.2. Diurnal changes in evaporation

Diurnal evaporation fluctuations during the desiccation stage reflect changing evaporative potential and water availability (Figure 6). The subtle morning increase in evaporation, which has been documented in other saline pans (Malek & Bingham, 1990; Sanford & Wood, 2001), was interpreted as the evaporation of groundwater from the overnight rehydration of the salt crust (Malek & Bingham, 1990). The 18:00 MST peak in evaporation is associated with the diurnal peak in groundwater level and temperature. This evaporation peak suggests that some of the groundwater from daily water-level fluctuations increases near-surface water availability. The 23:00 MST peak in evaporation is associated with the day's highest windspeed.

5.3. The flooding-evaporation-desiccation cycle

Saline pan sediments are interpreted through the flooding-evapoconcentration-desiccation cycle. This cycle is enhanced through evaporative and hydrological observations (Bowen et al., 2017; Lowenstein & Hardie, 1985). The desiccation stage describes periods when the surface is dry and albedo is high. Bowen *et al.* (2017) used the Standardized Precipitation Evaporation Index [(precipitation – evaporation)/variance] to calculate if the surface was in the flooding, evapoconcentration, or desiccation stage. When this index uses potential evaporation, it reflects seasonal trends in flooding and desiccation. However, when estimated evaporation is used in this index, many more months have a positive water balance, suggesting longer flooding periods or uptake of precipitation into the subsurface (Figure 4B and C). An alternative method to interpret these stages is with albedo. Rapidly declining albedo indicates flooding, increasing albedo indicates evapoconcentration, and a constant elevated albedo indicates the desiccation stage.

5.4. Saline pan water balance

There are three endmembers for the natural water budget at BSF: (1) the system is water neutral, with evaporation equaling precipitation, (2) rainfall exceeds evaporation, and (3) evaporation exceeds precipitation.

5.4.1. Water addition

Precipitation is the primary water input BSF. If anthropogenic brine, introduced as part of a mining mitigation project, is ~10-80% of the annual water contributed to the southwestern part of BSF (distributed over 20-50 km^2, Figure S2). Water inputs from snow or surface condensation such as dew, which would further decrease the calculated volume of groundwater evaporation, were assumed to be negligible in this study. If introduced brine and precipitation were evenly distributed over a 120 km^2 area, precipitation is 90 to 100% of BSF's annual recharge, with the remaining water being anthropogenically introduced. Past studies indicated other inputs such as vertical water fluxes, overland flow, or lateral groundwater movement are <1% of the incoming water budget at BSF (Lines, 1979; Mason & Kipp, 1998).

The distribution of surface water at BSF is uneven. Water accumulates in the low-lying ephemeral western pond. When the surface is flooded, precipitation can flow downhill to this pond. The seasonal pond increases evaporation at the weather station study site only when it extends to the weather station or when wind redistributes surface water over the playa (Bowen et al., 2017; Craft & Horel, 2019). Contributions to the pond from anthropogenic brine appear to have had a negligible impact on measured evaporation at the study location. If anthropogenic brine were significant at the study location, evaporation would exceed precipitation when the surface was wet, which was not observed. If evaporation from the western pond were included in estimating BSF's annual water budget, the ratio of evaporation to precipitation would increase. Lateral subsurface flow at the study location is considered negligible because of the site's low topography and groundwater's potentiometric surface is a local high near the study location.

5.4.2. Water removal

Water is currently removed from the saline pan by evaporation, groundwater extraction for potash production, and surface and subsurface flow away from the site (Mason & Kipp, 1998). Overland flow redistributes and concentrates water at the western part of BSF. However, this only occurs when the water level is near the surface. Removal of surface or groundwater would increase the local ratio of precipitation to evaporation (which is suggested by the E_eLow evaporation model).

Evaporation was previously estimated to contribute to 80% of BSF's annual discharge (Mason & Kipp, 1998). Uncertainties with the evaporation calculation are whether albedo and evaporation continue to scale consistently in the winter and if the consistency of the year-to-year albedo value relative to surface moisture. This relationship between albedo surface moisture is most important when the surface is wet and evaporation is high. Kampf *et al.* (2005) found that albedo can be lower in the more arid, dry parts of a saline crust, demonstrating that the relationship between albedo and evaporation deteriorates under extended aridity. Cumulative evaporation estimated with the artificial neural network was within 5% of the cumulative rainfall. These values show that most of the study site's water budget is contributable to evaporation and precipitation. The net annual water budget at BSF's center during this study was 0.5 ±1.5 cm y^{-1} (Figure 4A). Evaporation from the desiccated surface was 3-10 times lower than that previously estimated by Mason and Kipp (1998) using Bowen-ratio energy balance systems. Mason and Kipp corrected for this in their calibrated model of BSF's water budget, with precipitation exceeding evaporation by 15%, which aligns best with E_eLow evaporation model (precipitation is 10% greater than evaporation).

5.4.3. Anthropogenic impacts upon the water balance

Anthropogenic water removal for potash production is two to three times less than anthropogenic water introduced for mining mitigation (3-5% of annual discharge). However, added water is more available for evaporation, dampening its offset on the total groundwater volume. Furthermore, brine is removed from and introduced to different parts of BSF. Groundwater is extracted year-round, while brine is only introduced in the winter. Removal of groundwater for potassium production lowered well water levels near the extraction ditches, this signal is most evident in thermal-efficiency-corrected groundwater levels (Figure S2).

The impact of brine extraction on groundwater levels at BSF's center is indiscernible. The monthly average water level at BSF's center is consistent between March to September from year to year, regardless of the volume of monthly groundwater extraction during the study period. Decreases to groundwater levels by wound increase uptake of precipitation into the ground, creating water balances where precipitation exceeds evaporation, which was indicated by E_eLow evaporation and BSF's calibrated mass balance model (Mason & Kipp, 1998).

5.5. Implications for evaporite growth and dissolution

These and prior observations of saline-pan evaporation rates and surface features indicate that once a salt crust has formed and desiccated, evaporite growth is slow to negligible (Bernau & Bowen, 2021; Kampf et al., 2005). Groundwater evaporation is minimal once a crust has desiccated, indicating that salt crusts stabilize and preserve groundwater levels, indirectly stabilizing the surface. Without saline crusts, playas become ablation surfaces, creating significant dust sources (Rosen, 1994).

There must be a significant upward gradient for groundwater flow or lateral water input for saline pans to form primarily from groundwater. Currently BSF does not receive such fluxes

(Kipnis & Bowen, 2018; Mason & Kipp, 1998). As Rosen suggested (1994), preservation of evaporite systems is unlikely unless they are actively fed from external water sources and are in tectonic settings that support their accumulation and preservation. Alternatively, under little water input, these systems form very slowly or become deflation surfaces. Kampf *et al.* (2005) determined that preserved subaerially-formed efflorescent crusts at Salar de Atacama could have formed from a desiccated saline pan surface at net evaporation rates of 2 mm y^{-1}.

The sediments in saline pans suggest that most evaporite deposition occurs under conditions when there is enough surface moisture available for evaporation and evaporation exceeds precipitation. This moisture also decreases the surface albedo, increasing the absorption of solar energy (Lowenstein & Hardie, 1985). Under wetter conditions in the past, overland flow into BSF from the surrounding area would have contributed additional solutes to BSF by dissolving and transporting efflorescent crusts. By directly and indirectly reducing groundwater levels and water availability for evaporation (Marazuela et al., 2020), anthropogenic activities alter the balance between water input and evaporation within saline pans, leading growing saline pans to stabilize and stable saline pans to decline over time. Similiarly, global warming may also influence some saline pans by reducing water inputs into saline pans and increasing halite solubility through groundwater warming. Therefore, changes saline pans extent over time are indicators of regional trends and changes in groundwater availability.

6. Conclusions

Evaporation estimates made with an ensemble of methods demonstrate that the center of the Bonneville Salt Flats saline pan is water neutral to slightly water positive. Precipitation equals or exceeds evaporation at the center of this saline pan. Limited evaporation stabilized the local water table, periods with positive water balances contributed to the crust’s gradual dissolution over the past century. Sedimentologically, the current neutral water balance indicates the limited capability of groundwater evaporation to contribute to evaporite deposition in modern and ancient saline pans.

The methods utilized and evaluated in this work demonstrate that saline pan evaporative fluxes can be estimated with inexpensive micro-meteorological equipment or groundwater level monitors, but that calibration of these approaches with robust eddy flux station measurements is needed. Understanding saline pan processes, such as the inverse correlation between surface moisture and albedo and the positive correlation between ground temperature changes and groundwater level, is critical to utilizing these methodologies and interpreting saline pans.

Saline pan landscapes are dynamic and rapidly evolve in response to climate change and changes in water and mineral balances. Water extraction alters the water balance. Lowered groundwater levels lead to a decrease to cessation in surface evaporite growth. Evaporite crust loss can increase dust production potential. Long-term multi-parameter monitoring of these systems would allow us to gain new insights and understand how these systems will change in response to environmental stressors and how these changes will affect water supplies to dust sources. Furthering our understanding of saline pans' dynamism will enable us to effectively interpret and use these dynamic landscapes as sensitive indicators of regional hydrological fluctuations.

Acknowledgments

We thank Ross Petersen, Nipun Gunawardena, Alex Bingham, Alexei Perelet, Jory Lerback, Elliot Jagniecki, Boe Erickson, and Mark Radwin for assisting us in the field. This work developed through conversations and discussions with Ciarian Harmon, Tianqi Liu, Jason Kelley, and two anonymous readers. We thank Dave Bowling and Heather Holmes for sharing their equipment with us. This work was made possible with former BLM West Desert District office staff's support, including Kevin Oliver, Matt Preston, Mike Nelson, Cheryl Johnson, Steve Allen, and Roxanne Tea. Russ Draper support was essential for this project's success. An NSF Coupled Natural Human Systems Award #1617473 to Brenda Bowen and a University of Utah Global Change and Sustainability Center Graduate Student Research Grant funded this research. The authors and their affiliations do not have any real or perceived financial conflicts in performing this research.

Data Availability Statement

The data that support the findings of this study are openly available in Zenodo at https://doi.org/10.5281/zenodo.4171332, https://doi.org/10.5281/zenodo.4268710, and https://doi.org/10.5281/zenodo.5634172. The code that supports this work is archived at https://doi.org/10.5281/zenodo.5671739.

References

Allen, R. G., Pereira, L. S., Raes, D., & Smith, M. (1998). *FAO Irrigation and Drainage Paper No. 56. Irrigation and Drainage* (Vol. 300). Rome, Italy. https://doi.org/10.1016/j.eja.2010.12.001

Allison, G. B., & Barnes, C. J. (1985). Estimation of evaporation from the normally "dry" Lake Frome in South Australia. *Journal of Hydrology*, *78*(3–4), 229–242. https://doi.org/10.1016/0022-1694(85)90103-9

Benison, K. C., & Bowen, B. B. (2006). Acid saline lake systems give clues about past environments and the search for life on Mars. *Icarus*, *183*(1), 225–229. https://doi.org/10.1016/j.icarus.2006.02.018

Benison, K. C., & Karmanocky, F. J. (2014). Could microorganisms be preserved in Mars gypsum? Insights from terrestrial examples. *Geology*, *42*(7), 615–617. https://doi.org/10.1130/G35542.1

Bernau, J., & Bowen, B. B. (2020). Time lapse imagery and field photos of the surface of the Bonneville Salt Flats. https://doi.org/10.5281/zenodo.4171332

Bernau, J., & Bowen, B. B. (2021). Depositional and early diagenetic characteristics of modern saline pan deposits at the Bonneville Salt Flats, Utah, USA. *Sedimentology*, sed.12861. https://doi.org/10.1111/sed.12861

Bethke, C. M. (2013). *Geochemical and Biogeochemical Reaction Modeling*. *Journal of Chemical Information and Modeling* (Vol. 53). Cambridge, UK: Cambridge University Press.

Boutt, D. F., Hynek, S. A., Munk, L. A., & Corenthal, L. G. (2016). Rapid recharge of fresh water to the halite-hosted brine aquifer of Salar de Atacama, Chile. *Hydrological Processes*, *30*(25), 4720–4740. https://doi.org/10.1002/hyp.10994

Bowen, B. B., Kipnis, E. L., & Raming, L. W. (2017). Temporal dynamics of flooding, evaporation, and desiccation cycles and observations of salt crust area change at the Bonneville Salt Flats, Utah. *Geomorphology*, *299*, 1–11. https://doi.org/10.1016/j.geomorph.2017.09.036

Bowen, B. B., Kipnis, E. L., & Pechmann, J. M. (2018). Observations of salt crust thickness change at the Bonneville Salt Flats from 2003-2016. In S. H. Emerman, B. B. Bowen, S. Simmons, & S. Schamel (Eds.), *Geofluids of Utah* (47th ed., pp. 247–285). Utah Geological Association Publication.

Bowen, B. B., Bernau, J., Kipnis, E., Lerback, J., Wetterlin, L., & Kleba, B. (2018). The making of a perfect racetrack at the Bonneville Salt Flats. *The Sedimentary Record*, *16*(2), 4–11.

de Bruin, H., & Holstag, A. (1982). A simple parameterization of surface fluxes of sensible and latent heat during daytime compared with the Penman–Monteith concept. *Journal of Applied Meteorology and Climatology*, *21*(1), 1610–1621.

Calder, I. R., & Neal, C. (1984). Evaporation from saline lakes: A combination equation approach. *Hydrological Sciences Journal*, *29*(1), 89–97. https://doi.org/10.1080/02626668409490924

Chapman, S., & Lindzen, R. S. (1970). Atmospheric tides : thermal and gravitational, 212.

Costelloe, J. F., Matic, V., Western, A. W., Walker, J. P., & Tyler, M. (2011). Field estimates of groundwater discharge - Great Artesian Basin, South Australia. *MODSIM 2011 - 19th International Congress on Modelling and Simulation*, (December), 2100–2106.

Craft, K. M., & Horel, J. D. (2019). Variations in surface albedo arising from flooding and desiccation cycles on the Bonneville Salt Flats, Utah. *Journal of Applied Meteorology and Climatology*, *58*(4), 773–785. https://doi.org/10.1175/JAMC-D-18-0219.1

Crosbie, R. S., Binning, P., & Kalma, J. D. (2005). A time series approach to inferring groundwater recharge using the water table fluctuation method. *Water Resources Research*, *41*(1), 1–9. https://doi.org/10.1029/2004WR003077

Crosbie, R. S., Doble, R. C., Turnadge, C., & Taylor, A. R. (2019). Constraining the Magnitude and Uncertainty of Specific Yield for Use in the Water Table Fluctuation Method of Estimating Recharge. *Water Resources Research*, *55*(8), 7343–7361. https://doi.org/10.1029/2019WR025285

Van Dam, R. L., Simmons, C. T., Hyndman, D. W., & Wood, W. W. (2009). Natural free convection in porous media: First field documentation in groundwater. *Geophysical Research Letters*, *36*(11), 1–5. https://doi.org/10.1029/2008GL036906

DeMeo, G. A., Laczniak, R. J., Boyd, R. A., Smith, J. L., & Nylund, W. E. (2003). *Estimated ground-water discharge by evapotranspiration from Death Valley, California, 1997–2001*. Carson City, NV.

Duffy, C. J., & Al-Hassan, S. (1988). Groundwater circulation in a closed desert basin: Topographic scaling and climatic forcing. *Water Resources Research*, *24*(10), 1675–1688. https://doi.org/10.1029/WR024i010p01675

Duke, H. R. (1972). Capillary Properties of Soils - Influence Upon Specific Yield. *Transactions of the ASAE*, *15*(4), 0688–0691. https://doi.org/10.13031/2013.37986

Fan, Y., Duffy, C. J., & Oliver, D. S. (1997). Density-driven groundwater flow in closed desert basin: Field investigations and numerical experiments. *Journal of Hydrology*, *196*, 139–184. https://doi.org/10.1016/S0022-1694(96)03292-1

Garcia, C. A., Huntington, J. M., Buto, S. G., Moreo, M. T., Smith, J. L., & Andraski, B. J. (2015). Groundwater Discharge by Evapotranspiration, Dixie Valley, West-Central Nevada, March 2009–September 2011. *U.S. Geological Survey Professional Paper*, (1805), 1–90. https://doi.org/http://dx.doi.org/10.3133/pp1805

Gerla, P. J. (1992). The relationship of water-table changes to the capillary fringe, evapotranspiration, and precipitation in intermittent wetlands. *Wetlands*, *12*(2), 91–98. https://doi.org/10.1007/BF03160590

Gillham, R. W. (1984). The capillary fringe and its effect on water-table response. *Journal of Hydrology*, *67*(1–4), 307–324. https://doi.org/10.1016/0022-1694(84)90248-8

Gonthier, G. J. (2007). A Graphical Method for Estimation of Barometric Efficiency from Continuous Data — Concepts and Application to a Site in the Piedmont , Scientific Investigation Report 2007-5111 Prepared in cooperation with the U.S. Air Force Aeronautical Systems Center, M. *U. S. Geological Survey Scientific Investigation Report*

2007-5111, 38.

Hang, C., Nadeau, D. F., Jensen, D. D., Hoch, S. W., & Pardyjak, E. R. (2016). Playa soil moisture and evaporation dynamics during the MATERHORN field program. *Boundary-Layer Meteorology*, *159*(3), 521–538. https://doi.org/10.1007/s10546-015-0058-0

Healy, R. W., & Cook, P. G. (2002). Using groundwater levels to estimate recharge. *Hydrogeology Journal*, *10*(1), 91–109. https://doi.org/10.1007/s10040-001-0178-0

Heliotis, F. D., & DeWitt, C. B. (1987). Rapid Water Table Responses to Rainfall in a Northern Peatland Ecosystem. *JAWRA Journal of the American Water Resources Association*, *23*(6), 1011–1016. https://doi.org/10.1111/j.1752-1688.1987.tb00850.x

Horel, J., Splitt, M., Dunn, L., Pechmann, J., White, B., Ciliberti, C., et al. (2002). Mesowest: Cooperative mesonets in the western United States. *Bulletin of the American Meteorological Society*, *83*(2), 211–225.

Huntington, J. M., Garcia, A., & Rosen, M. R. (2014). Hydrogeologic framework and occurrence, movement, and chemical characterization of groundwater in Dixie Valley, west-central Nevada. *U.S. Geological Survey Scientific Investigations Report*, *2014–5152*, 60. https://doi.org/http://dx.doi.org/10.3133/sir20145152

Jackson, T. R., Halford, K. J., Gardner, P. M., & Garcia, A. (2018). Evaluating micrometeorological estimates of groundwater discharge from Great Basin desert playas. *Groundwater*, *56*(6), 909–920. https://doi.org/10.1111/gwat.12647

Jacobson, G., & Jankowski, J. (1989). Groundwater-discharge processes at a central Australian playa. *Journal of Hydrology*, *105*(3–4), 275–295. https://doi.org/10.1016/0022-1694(89)90109-1

Jensen, D. D., Nadeau, D. F., Hoch, S. W., & Pardyjak, E. R. (2016). Observations of near-surface heat-flux and temperature profiles through the early evening transition over contrasting surfaces. *Boundary-Layer Meteorology*, *159*(3), 567–587. https://doi.org/10.1007/s10546-015-0067-z

Kampf, S. K., & Tyler, S. W. (2006). Spatial characterization of land surface energy fluxes and uncertainty estimation at the Salar de Atacama, Northern Chile. *Advances in Water Resources*, *29*(2), 336–354. https://doi.org/10.1016/j.advwatres.2005.02.017

Kampf, S. K., Tyler, S. W., Ortiz, C. A., Muñoz, J. F., & Adkins, P. L. (2005). Evaporation and land surface energy budget at the Salar de Atacama, northern Chile. *Journal of Hydrology*, *310*(1–4), 236–252. https://doi.org/10.1016/j.jhydrol.2005.01.005

Kang, M., Ichii, K., Kim, J., Indrawati, Y. M., Park, J., Moon, M., et al. (2019). New gap-filling strategies for long-period flux data gaps using a data-driven approach. *Atmosphere*, *10*(10), 1–18. https://doi.org/10.3390/atmos10100568

Kelley, J. (2020). Assessment and correction of solar radiation measurements with simple neural networks. *Atmosphere*, *11*(11). https://doi.org/10.3390/atmos11111160

Kelley, J., & Pardyjak, E. R. (2019). Using neural networks to estimate site-specific crop evapotranspiration with low-cost sensors. *Agronomy*, *9*(2). https://doi.org/10.3390/agronomy9020108

Kelley, J., Mccauley, D., Alexander, G. A., Iv, W. F. G., Siegfried, R., & Oldroyd, H. J. (2020). Using machine learning to integrate on-farm sensors and agro-meteorology networks into site-specific decision support, *63*(5), 1427–1439.

Kipnis, E. L., & Bowen, B. B. (2018). Observations of salt crust change from 1960-2016 and the role of humans as geologic agents at the Bonneville Salt Flats, Utah. In S. H. Emerman, B. B. Bowen, S. Simmons, & S. Schamel (Eds.), *Geofluids of Utah* (47th ed., pp. 287–301). Utah Geological Association Publication.

Kipnis, E. L., Bowen, B. B., Hutchings, S. J., Hynek, S. A., & Benison, K. C. (2020). Major ion geochemistry in Na-Ca-Mg-K-Cl-SO4 brines using portable X-ray fluorescence spectrometry. *Chemical Geology*, 135577. https://doi.org/https://doi.org/10.1016/j.chemgeo.2020.119865

Lerback, J. C., Hynek, S. A., Bowen, B. B., Bradbury, C. D., Solomon, D. K., & Fernandez, D. P. (2019). Springwater provenance and flowpath evaluation in Blue Lake, Bonneville basin, Utah. *Chemical Geology*, *529*(April), 119280. https://doi.org/10.1016/j.chemgeo.2019.119280

Li, X., & Shi, F. (2019). The effect of flooding on evaporation and the groundwater table for a salt-crusted soil. *Water (Switzerland)*, *11*(5). https://doi.org/10.3390/w11051003

Lines, G. C. (1978). *Selected ground-water data, Bonneville Salt Flats and Pilot Valley, western Utah*. *UGS*. https://doi.org/10.1007/978-94-017-4477-5_19

Lines, G. C. (1979). Hydrology and surface morphology of the Bonneville Salt Flats and Pilot Valley playa, Utah. *Geological Survey Water-Supply Paper 2057*, (2057), 1–107.

Lowenstein, T. K., & Hardie, L. A. (1985). Criteria for the recognition of salt-pan evaporites. *Sedimentology*, *32*(5), 627–644. https://doi.org/10.1111/j.1365-3091.1985.tb00478.x

Lowenstein, T. K., Spencer, R. J., & Pengxi, Z. (1989). Origin of ancient potash evaporites: Clues from the modern nonmarine Qaidam Basin of western China. *Science*, *245*(4922), 1090–1092.

Lv, M., Xu, Z., Yang, Z. L., Lu, H., & Lv, M. (2021). A Comprehensive Review of Specific Yield in Land Surface and Groundwater Studies. *Journal of Advances in Modeling Earth Systems*, *13*(2), 1–24. https://doi.org/10.1029/2020MS002270

Macumber, P. G. (1991). *Interaction between groundwater and surface systems in Northern Victoria*. East Melbourne, Victoria, Australia: Department of Conservation and Environment.

Malek, E., & Bingham, G. E. (1990). Evapotranspiration from the margin and moist playa of a closed desert valley. *Journal of Hydrology*, *120*, 15–34.

Marazuela, M. A., Vázquez-Suñé, E., Ayora, C., García-Gil, A., & Palma, T. (2019a). Hydrodynamics of salt flat basins: The Salar de Atacama example. *Science of the Total Environment*, *651*, 668–683. https://doi.org/10.1016/j.scitotenv.2018.09.190

Marazuela, M. A., Vázquez-Suñé, E., Ayora, C., García-Gil, A., & Palma, T. (2019b). The effect of brine pumping on the natural hydrodynamics of the Salar de Atacama: The damping capacity of salt flats. *Science of the Total Environment*, *654*, 1118–1131. https://doi.org/10.1016/j.scitotenv.2018.11.196

Mardones, L. (1998). *Fluxes and evolution of saline solutions in the hydrological systems of Ascotan and Atacama salars*. University of Paris.

Marticorena, B., Kardous, M., Bergametti, G., Callot, Y., Chazette, P., Khatteli, H., et al. (2006). Surface and aerodynamic roughness in arid and semiarid areas and their relation to radar backscatter coefficient. *Journal of Geophysical Research: Earth Surface*, *111*(3). https://doi.org/10.1029/2006JF000462

Mason, J. L., & Kipp, K. L. (1998). Hydrology of the Bonneville Salt Flats, northwestern Utah, and simulation of ground-water flow and solute transport in the shallow-brine aquifer. *U.S. Geological Survey Professional Paper 1585*, 108.

Mason, J. L., Brothers, W. C., Gerner, L. J., & Muir, P. S. (1995). *Selected hydrologic data for the Bonneville Salt Flats and Pilot Valley, western Utah, 1991-93*. *U.S. Geological Survey Open-File Report 95-104*. Salt Lake City, Utah.

MathWorks. (2020a). Deep Learning Toolbox. Natick, MA, USA: The Mathworks Inc.

MathWorks. (2020b). Matlab R2020b. Natick, MA, USA.

McMillan, T. C., Rau, G. C., Timms, W. A., & Andersen, M. S. (2019). Utilizing the Impact of Earth and Atmospheric Tides on Groundwater Systems: A Review Reveals the Future Potential. *Reviews of Geophysics*, *57*(2), 281–315. https://doi.org/10.1029/2018RG000630

Menking, K. M., Anderson, R. Y., Brunsell, N. A., Allen, B. D., Ellwein, A. L., Loveland, T. A., & Hostetler, S. W. (2000). Evaporation from groundwater discharge playas, Estancia Basin, central New Mexico. *Global and Planetary Change*, *25*(1–2), 133–147. https://doi.org/10.1016/S0921-8181(00)00025-4

Meyer, F. A. (1960). Effect of temperature on ground-water levels. *Journal of Geophysical Research*, *65*(6), 1747–1752. https://doi.org/10.2118/65-04-09

Mor, Z., Assouline, S., Tanny, J., Lensky, I. M., & Lensky, N. G. (2018). Effect of water surface salinity on evaporation: The case of a diluted buoyant plume over the Dead Sea. *Water Resources Research*, *54*(3), 1460–1475. https://doi.org/10.1002/2017WR021995

Munk, L. A., Boutt, D. F., Moran, B. J., McKnight, S. V., & Jenckes, J. (2021). Hydrogeologic and geochemical distinctions in freshwater-brine systems of an Andean salar. *Geochemistry, Geophysics, Geosystems*. https://doi.org/10.1029/2020gc009345

Nachshon, U., Weisbrod, N., Dragila, M. I., & Grader, A. (2011). Combined evaporation and salt precipitation in homogeneous and heterogeneous porous media. *Water Resources Research*, *47*(3), 1–16. https://doi.org/10.1029/2010WR009677

Nachshon, U., Weisbrod, N., Katzir, R., & Nasser, A. (2018). NaCl crust architecture and its impact on evaporation: Three-dimensional insights. *Geophysical Research Letters*, *45*(12), 6100–6108. https://doi.org/10.1029/2018GL078363

Nield, J. M., King, J., Wiggs, G. F. S., Leyland, J., Bryant, R. G., Chiverrell, R. C., et al. (2013). Estimating aerodynamic roughness over complex surface terrain. *Journal of Geophysical Research Atmospheres*, *118*(23), 12948–12961. https://doi.org/10.1002/2013JD020632

Nield, J. M., Bryant, R. G., Wiggs, G. F. S., King, J., Thomas, D. S. G., Eckardt, F. D., & Washington, R. (2015). The dynamism of salt crust patterns on playas. *Geology*, *43*(1), 31–

34. https://doi.org/10.1130/G36175.1

Post, V., Kooi, H., & Simmons, C. (2007). Using hydraulic head measurements in variable-density ground water flow analyses. *Ground Water*, *45*(6), 664–671. https://doi.org/10.1111/j.1745-6584.2007.00339.x

Read, E. K., Carr, L., De Cicco, L., Dugan, H. A., Hanson, P. C., Hart, J. A., et al. (2017). Water quality data for national-scale aquatic research: The Water Quality Portal. *Water Resources Research*, *53*(2), 1735–1745. https://doi.org/10.1002/2016WR019993

Robinson, E. S., & Bell, R. T. (1971). Tides in confined well- aquifer systems. *J Geophys Res*, *76*(8), 1857–1869. https://doi.org/10.1029/jb076i008p01857

Rosen, M. R. (1994). The importance of groundwater in playas: A review of playa classifications and the sedimentology and hydrology of playas. *Geological Society of America Special Papers*, *289*(January 1994), 1–18. https://doi.org/10.1130/SPE289-p1

Sanford, W. E., & Wood, W. W. (2001). Hydrology of the coastal sabkhas of Abu Dhabi, United Arab Emirates. *Hydrogeology Journal*, *9*(4), 358–366. https://doi.org/10.1007/s100400100137

Schulz, S., Horovitz, M., Rausch, R., Michelsen, N., Mallast, U., Köhne, M., et al. (2015). Groundwater evaporation from salt pans: Examples from the eastern Arabian Peninsula. *Journal of Hydrology*, *531*, 792–801. https://doi.org/10.1016/j.jhydrol.2015.10.048

Sieland, R. (2014). Hydraulic investigations of the Salar de Uyuni, Bolivia. *FOG - Freiberg Online Geoscience*, *37*(December 2014).

Stull, R. (2012). *An introduction to boundary layer meteorology* (Vol. 13). Springer Science & Business Media. https://doi.org/10.4267/2042/53468

Turk, L. J. (1970). Evaporation of brine: A field study on the Bonneville Salt Flats, Utah. *Water Resources Research*, *6*(4), 1209–1215. https://doi.org/10.1029/WR006i004p01209

Turk, L. J. (1973). *Hydrogeology of the Bonneville Salt Flats*. Salt Lake City, UT: Utah Geological and Mineral Survey.

Turk, L. J. (1975). Diurnal fluctuations of water tables induced by atmospheric pressure changes. *Journal of Hydrology*, *26*, 1–16.

Turk, L. J., Davis, S. N., & Bingham, C. P. P. (1973). Hydrogeology of lacustrine sediments, Bonneville Salt Flats, Utah. *Economic Geology*, *68*(1), 65–78. https://doi.org/10.2113/gsecongeo.68.1.65

Turnadge, C., Crosbie, R. S., Barron, O., & Rau, G. C. (2019). Comparing Methods of Barometric Efficiency Characterization for Specific Storage Estimation. *Groundwater*, *57*(6), 844–859. https://doi.org/10.1111/gwat.12923

Tyler, S. W., Kranz, S., Parlange, M. B., Albertson, J., Katul, G. G., Cochran, G. F., et al. (1997). Estimation of groundwater evaporation and salt flux from Owens Lake, California, USA. *Journal of Hydrology*, *200*(1–4), 110–135. https://doi.org/10.1016/S0022-1694(97)00007-3

Tyler, S. W., Muñoz, J. F., & Wood, W. W. (2006). The response of playa and sabkha hydraulics and mineralogy to climate forcing. *Ground Water*, *44*(3), 329–338. https://doi.org/10.1111/j.1745-6584.2005.00096.x

Ullman, W. J. (1985). Evaporation rate from a salt pan: Estimates from chemical profiles in near-surface groundwaters. *Journal of Hydrology*, *79*(3–4), 365–373. https://doi.org/10.1016/0022-1694(85)90066-6

Walton, W. C. (1970). *Groundwater resource evaluation*. McGraw-Hill series in water resources and environmental engineering. https://doi.org/10.1016/0022-1694(71)90082-5

van Weert, F., & van der Gun, J. (2012). Saline and Brackish groundwater at shallow and intermediate depths: Genesis and World Wide Occurrence. *2012 Congress of the Canadian Branch of the International Association of Hydrogeologists (IAH)*, 1–9. Retrieved from https://www.un-igrac.org/es/resource/saline-and-brackish-groundwater-shallow-and-intermediate-depths-genesis-and-world-wide

Wooding, R. A., Tyler, S. W., White, I., & Anderson, P. A. (1997). Convection in groundwater below an evaporating salt lake: 1. Onset of instability. *Water Resources Research*, *33*(6), 1219–1228. https://doi.org/10.1029/96WR03534

Wurtsbaugh, W. A., Miller, C., Null, S. E., Justin De Rose, R., Wilcock, P., Hahnenberger, M., et al. (2017). Decline of the world's saline lakes. *Nature Geoscience*, *10*(11), 816–823. https://doi.org/10.1038/ngeo3052

AGU PUBLICATIONS

Water Resources Research

Supporting Information for

Diurnal to Seasonal Dynamics of Groundwater, Evaporation, and Hydrology Fluctuations at the Bonneville Salt Flats Saline Pan

BJ.A. Bernau[1], B. B. Bowen[1,2], E. R. Pardyjak[3], and E. L. Kipnis[1]

[1]Geology and Geophysics, University of Utah, Salt Lake City, UT, USA; [2]Global Change and Sustainability Center, University of Utah, Salt Lake City, UT, USA; [3]Mechanical Engineering, University of Utah, Salt Lake City, UT, USA

Contents of this file

Text S1 to S3
Figures S1 to S9

Introduction

This file contains supporting information describing data sources, data processing steps, and theoretical background, as well as supplemental figures. The data quality control, gap-filling, and Matlab (MathWorks, 2020b) analyses code used for this study is available at https://doi.org/10.5281/zenodo.5671739 and the datasets that support this work are archived at https://doi.org/10.5281/zenodo.5634172 and https://doi.org/10.5281/zenodo.4268710. These datasets consist of modern and historical meteorological and groundwater measurements.

Supporting Information

Text S1. Meteorological Data

Meteorological measurements and products are archived at https://doi.org/10.5281/zenodo.5634172. The data quality control, gap-filling, and Matlab (MathWorks, 2020b) analyses code used for this study are archived at https://doi.org/10.5281/zenodo.5671739.

Meteorological measurements and surface observations

Historical meteorological measurements from the Bonneville Salt Flats and the surrounding area were reported by Lines (1979) and Mason and Kipp (1998). Additional measurements from Wendover, Utah, were collected from the National Oceanic and Atmospheric Administration (NOAA) Climate Data Online Portal. Weather station data at BSF was collected from the MesoWest weather station data repository (https://mesowest.utah.edu/, station ID: BFLAT) (Horel et al., 2002).

These measurements were used to examine the spatial and temporal heterogeneity of precipitation and evaporation in the area surrounding BSF (Figure S2). Precipitation in 2020 was four times lower than the preceding years of 2017 to 2019. The year of 2019 was 40% wetter than the next wettest year during the study period of 2016 to 2021.

Eddy-Covariance Data and Aerodynamic Roughness

The eddy-covariance equipment was oriented to the northwest and installed at the height of 2.57 m from May to August 2018. Eddy-covariance data available at https://doi.org/10.5281/zenodo.5634172 and the code used to determine the aerodynamic roughness length is available at https://doi.org/10.5281/zenodo.5671739.

The aerodynamic roughness length (Z_o) (meters) was determined with sonic anemometer data collected from May to August 2018 with equation S1-1. Equation S1-1 is rearranged to solve for Z_o in equation S1-2; the data is filtered where L is > 100 m, such that $\Psi_m(\frac{Z}{L})$ approaches zero (Stull, 2012).

$$\frac{\overline{m}}{u_*} = 1/K(\ln\left(\frac{Z}{Z_o}\right) + \Psi_m\left(\frac{Z}{L}\right)) \quad \text{(S1-1)}$$

$$Z_o = Z/\exp\,(K\frac{\overline{m}}{u_*}) \quad \text{(S1-2)}$$

Where $\overline{m}$ is wind speed (m/s) filtered to only include wind speeds between 2-6 m/s, μ_* is the friction velocity (m/s), K is the von Karman Constant (0.4), Z is the measurement height (m), Ψ_m is the stability function, and L is the Monin-Obukhov length scale. The median value of Z_o at BSF was $5.4*10^{-4}$ m.

Meteorological data gap filling

Outgoing and net longwave radiometer measurements from November 24, 2019 to March 2, 2020 were removed from the dataset for quality control. Longwave radiation measurements were not available prior to the installation of the longwave radiometers on June 6, 2017. An artificial neural network was shown to estimate radiation effectively by Kelley (2020). The neural network (using the methods outlined in Text S3, and with the training inputs of air temperature, relative humidity, wind speed, incoming and outgoing shortwave radiation, and time of day) was used to fill data *gaps. The artificial neural network was more effective at estimating net longwave radiation than incoming longwave radiation (Figure S3). Incoming longwave radiation was calculated by subtracting the outgoing radiation from net longwave radiation.*

From June 9 to 11, 2019, the weather station did not log meteorological measurements. Temperature, humidity, air pressure, and incoming shortwave radiation measurement from this period were replaced with measurements made by the nearby DPG17 weather station (https://mesowest.utah.edu/, station ID: DPG17). Outgoing shortwave radiation and incoming and outgoing longwave radiation during this period were replaced with measured mean BSF radiation measurements from the preceding and proceeding days.

Imagery

The saline pan's surface properties and surface features changed over time with evaporite growth, dissolution, and alteration. Time-lapse imagery from the BFLAT weather station is available at http://home.chpc.utah.edu/~u0790486/wxinfo/cgi-bin/uunet_camera_explorer.cgi Camera: Bonneville Salt Flats, and, along with imagery from other locations at https://doi.org/10.5281/zenodo.4171331 (Bernau & Bowen, 2021). There are some gaps within the weather station-collected imagery because of equipment malfunctions. The camera view was shifted downward from April 7 to 11, 2018. The camera was non-functioning from February 7 to May 18, 2020.

Text S2. Estimated Evaporation Models

Estimated evaporation model results are available at https://doi.org/10.5281/zenodo.5634172 and code is available at https://doi.org/10.5281/zenodo.5671739.

Potential evaporation-based models

Water Activity

The water activity of BSF brines was estimated with geochemical modeling and previously derived empirical relationships between brine density and water activity for BSF brines (Turk, 1973). Water samples from BSF (Kipnis et al., 2020) were equilibrated with halite using the React module in Geochemist's Workbench (Bethke, 2013). The phrqpitz thermodynamic dataset was used. The water activity of brine equilibrated with halite was then calculated with the SpecE8 module. The mean calculated water activity in Geochemist's Workbench was 0.75 with a standard deviation <0.01.

The density of natural and anthropogenic BSF surface brines was used as an input for an equation derived from Turk's (1973) measurements of BSF brines. The average water activity calculated with method was 0.73 (standard deviation of 0.04). The maximum calculated water activity was 0.86. These results indicate that sustained surface brines at BSF have water activities between 0.73 to 0.75. A constant water activity of 0.74 was used in this research. Immediately after meteoric precipitation, BSF brine water activity is likely >0.74. Changes in water activity are buffered by dissolution of surface halite.

Penman equation evaporation

The potential evaporation calculated with the Penman equation (PE) and with the Calder and Neal (1984) water-activity corrected adaptation of the Penman equation (PE CN) are similar. The PE CN evaporation values were slightly lower (>20% less) than evaporation calculated with the unaltered Penman equation. The water activity corrected evaporation was used to create albedo-calibrated estimated evaporation values. The scaling correction values that are dependent on albedo and are used in the E_eHigh and E_eLow models are summarized in the table below.

Inputs used for albedo-calibrated estimated evaporation (E_eHigh and E_eLow) models

Albedo	*Evaporation estimation equation*	*K_c (scaling value)*
>0.37 (E_eHigh and E_eLow)	$E_e = K_{c1}$(PE CN)/albedo	$K_{c1} = 0.0788$
<0.37 (E_eHigh)	$E_e = K_{c2}$(PE CN)/albedo	$K_{c2} = 0.0570$
<0.37 (E_eLow)	$E_e = K_{c3}$(PE CN)	$K_{c3} = 0.0351$

Artificial neural network models

The MATLAB Deep Learning Toolbox (MathWorks, 2020a) was used to implement the artificial neural network used to estimate evaporation. The artificial neural network is structured such that each period is evaluated independently of the proceeding and preceding measurements. The artificial neural network consisted of two layers (a hidden training layer with 10 nodes and a single node output layer). It was trained using the Bayesian regularization backpropagation algorithm. This algorithm is implemented with the Levenberg-Marquardt optimization. The data was split randomly such that 70% of the dataset was used for training, and 30% was used for validation. Following Kelley and Pardyjak's (2019) methods, the 30-minute average values of weather station measurements were used as input values. These data were trained to replicate evaporation measured by the eddy-covariance method.

Different training inputs were used to test what inputs enhanced or decreased the quality of the artificial neural network model, as compared to the albedo-calibrated evaporation models (Figures S4 and S5). Using longwave radiation as an input improved artificial neural network evaporation outputs by making them more similar to the E_eLow model during known dry periods.

The generalizability of artificial neural network models to periods that were outside of training conditions was investigated by iteratively removing periods with low temperatures and high humidity values from the training dataset and comparing the model outputs (Figure S5). Removing lower temperatures from the training dataset led to higher evaporation estimates. This result indicates that the artificial neural network overestimated winter evaporation. This was corroborated by the difference between potential evaporation-based models of winter evaporation and the much higher winter evaporation estimates of the artificial neural network.

Text S3. Groundwater Data

Recent and historical measurements of groundwater levels, temperatures, water chemistry, anthropogenic brine fluxes, and well meta-data compiled from published data, the United States Geological Survey's national water information system (NWIS), and the Water Quality Portal are available at https://doi.org/10.5281/zenodo.4268710 (Bernau & Bowen, 2021; Kipnis & Bowen, 2018; Lines, 1978, 1979; Mason et al., 1995; Mason & Kipp, 1998; Read et al., 2017; Turk, 1973). The wells referred to in the main text as the 0.8 m and 3.5 m deep wells are identified as BLM-93C and BLM-93, respectively, in past publications. Supplemental figures incorporating current and historical groundwater data include Figures S2 and S6 to S9.

Continuous water levels from 2017 to 2021 were measured with non-vented pressure transducers. There were some data gaps from repositioning data loggers or loggers reaching data storage capacity. Groundwater levels were calculated by subtracting atmosphere pressure from the transducer-measured pressure. Where possible, groundwater measurements were corrected to be equivalent heads of a halite-saturated water column and were corrected for barometric efficiency. The effect of daily to seasonal temperature changes on groundwater level was quantified. Furthermore, the apparent specific yield of near surface sediments was estimated. The code used to perform these analyses is available at https://doi.org/10.5281/zenodo.5671739.

Equivalent head calculation

For flow calculations, head values for waters of differing density are often converted into equivalent heads of freshwater (Post et al., 2007). The water table at BSF's center is in direct contact with the evaporite crust, and is therefore halite-saturated. Therefore, to better estimate water table levels, head is estimated here by converting the measured head to an equivalent head of halite-saturated brine. The density for the 0.8 and 3.5-m deep wells was calculated using the equations' of state for these brines (Bernau & Bowen, 2021) with the soil temperature at 10 cm used as the temperature input (Figure S6). Calculated densities strongly reflected measured densities.

Although groundwater density changed throughout the year in both wells because of temperature and salinity changes, the equivalent head, when a constant density throughout the year was assumed, differed from the variable density equivalent head model by 0.5 to 1.2 cm (Figure S6). Because of this minor difference between methodologies, and the limited ground temperature and brine density measurements for many sites, groundwater density in each well was assumed to be constant when determining the equivalent head. When available, the well's brine's equation of state and a temperature range throughout the year was used to determine a representative average brine density; otherwise, the average measured density of the groundwater from a well was used.

Barometric efficiency correction

Air-pressure changes and other external forces impact water levels in wells (McMillan et al., 2019). There is differential loading of barometric pressure between the exposed well water and the aquifer's matrix and pore water in confined aquifers. This difference leads to an inverse relationship between barometric pressure and groundwater levels. The effect of air pressure on water level is quantified by a well's barometric efficiency (equation S3-1).

$$BE = 1 - \frac{dw}{db} \approx 1 - \frac{\Delta w}{\Delta b} \qquad \text{(S3-1)}$$

where barometric efficiency (BE) is equal to 1 minus the change in groundwater pressure (dw) relative to the change in barometric pressure (db). For the Bonneville Salt Flats, barometric pressure units were converted into an equivalent column of halite-saturated water. The water column measurements, reported as an equivalent head of halite-saturated brine, were then used as inputs to calculate barometric efficiency.

The median-of-ratios and linear regression time domain-based methods (as described in Turnadge et al., 2019) were used to determine the barometric efficiency BSF wells. The median-of-ratios was calculated by taking the median value of the ratio of the change in water level to the change in barometric pressure over a time period (Gonthier, 2007). The linear regression method determines the coefficient of the linear function where water level changes because of barometric pressure changes (Robinson & Bell, 1971). The time periods of change of one hour and one day were selected to test the impact of changing time period on the results.

Once the barometric efficiency was calculated it was applied to the dataset to determine what the water level would be without changes in barometric efficiency (Equations S3-2 and S3-3). The original water level and barometric efficiency corrected water level were then graphically assessed. If the application of barometric efficiency increased variability in measured water level, it was increased, in some cases to 1.

$$\Delta w_b = \ cumsum(((\frac{d}{dx}(b)) * (1 - BE)) \tag{S3-2}$$

where Δw_b is the change in water level originating from air pressure over the study interval relative to its starting point, $\frac{d}{dx}(b)$ is the change in air pressure (in units of an equivalent column of halite-saturated water) per unit time interval and BE is the barometric efficiency. The cumulative sum of this is calculated to determine how waster levels would change over time for changes in air pressure.

$$w_{BE} = \ w - \Delta w_b + mean(\Delta w_b)/2 \tag{S3-3}$$

where w_{BE} is the water level with the barometric efficiency signal removed, w is the original water level (as expressed in equivalent head of halite-saturated water). The effect air pressure on the water level at each moment is subtracted from the measured water level, because this would cause an offset in reported water elevation the mean value of the cumulative sum of water level change column is calculated and divided by two to determine the proper offset, which is added then added to the calculated water level at any moment. This methodology assumes that the barometric efficiency is invariable over time, which may not be the case for wells in unconfined aquifers.

For the 3.5 m well, the barometric efficiencies determined by the median-of-ratios and linear regression methods and with different time intervals were similar (0.59-0.61). The 0.8 m well's barometric efficiency value differed depending on if the one hour or one day time interval was used (from 0.51 to 0.86). Visual analysis of the barometric-corrected data for the 0.8 m well showed that water level data was more variable when a barometric efficiency <1 was considered; because of this, a barometric efficiency of 1 was assumed. If temperature was known to impact diurnal water levels fluctuations then only intervals of one day were used to determine well's barometric efficiency. The barometric efficiency of other BSF wells varied between 0.54 and 1. Wells screened within lacustrine sediments near BSF's center had barometric efficiencies between 0.54 and 0.60.

When the barometric correction was applied to the 3.5 m well, the resulting water level changes were similar to those observed in the 0.8 m well (Figure S6). The 3.5 m well's low barometric efficiency indicates that the lacustrine sediment-hosted aquifer in contact with the well has low permeability and poor connection with the atmosphere.

Thermal efficiency calculation and correction

Meyer (1960) first described the effect of temperature on water levels. Turk (1973) first described this effect at BSF. This effect is quantified and modeled here to identify intervals during which non-thermal processes impact water levels from seasonal to daily timescales (Figure S2).

Methodology

This methodology makes several simplifying assumptions about water levels at BSF. It assumes that the sediment column is uniform in porosity, so water level change scale linearly with temperature changes at all depths. It also assumes that temperature fluctuations are the primary control on water level changes, namely that there is no water movement in or out of the system. The effect of air pressure has also been removed by correcting for barometric efficiency. The dataset is limited to intervals that these assumptions hold. Finally, temperatures from a 10-cm depth soil probe were used as the input for these analyses to increase comparability between wells. The code used to perform these analyses is available at https://doi.org/10.5281/zenodo.5671739.

The thermal efficiency, TE (equation S3-4), was calculated by adapting the analytical framework for barometric efficiency (see prior section). The median-of-ratios was calculated by taking the median value of the ratio of the change in water level to the change in soil temperature over some time. The linear regression method determined the coefficient of the linear function where the water level changes as a function of temperature changes.

$$TE=\frac{\Delta wd}{\Delta T_{soil}} \qquad \text{(S3-4)}$$

where Δwd is the change in density and barometric efficiency corrected water depth (cm) and ΔT_{soil} is the temperature change(°C) from a 10-cm depth soil probe, and TE is the thermal efficiency.

Daily thermal efficiency values

The diurnal thermal efficiency was determined through two methods. The first method used linear regression and median-of-ratios approaches on hourly water level and temperature change periods. The second method used the median-of-ratios technique on the ratio of the daily range in soil temperature to the daily range in water level. Each month was analyzed individually using both methods to identify seasonal trends in temperature-controlled diurnal water level fluctuations.

The first method only worked with the 0.8 m deep well (BLM-93C) co-located with the soil temperature probe. This method showed that there are seasonal variations in the daily thermal efficiency. The thermal efficiency signal was strong with a high R^2 (>0.6) and a value between ~0.5 and 0.8 between May and October. This pattern reflects the correlation between diurnal water level fluctuation and maximum air temperature (Figure 6). This method was ineffective in other wells because of lags in heat transfer relating to well and water depth. Therefore, the second method was used to compare wells.

The median-of-ratios approach using daily ranges in water depth and soil temperature yielded similar results to the first method for the 0.8 m well. The median diurnal thermal efficiency of wells within the saline pan was found to be >0.25 to 0.5. The 0.8-m well was an outlier with a thermal efficiency of ~0.73. Wells to the west of the saline pan and at its northeastern edge had lower daily thermal efficiencies of 0.15 to <0.25.

Seasonal thermal efficiency values

Seasonal thermal efficiencies were determined using weekly and monthly periods of water level and temperature change. Using these more extended periods significantly limited the number of data points, so only the median-of-ratios method was used to determine seasonal thermal efficiencies. Because of the effect of non-thermal processes on water levels over these longer timescales, datasets were clipped to only the driest periods with the most notable temperature-controlled water level changes (typical August to December).

Data were plotted and then compared with observed changes in water level to qualitatively assess if calculated thermal efficiency values were recreating seasonal changes in water level. In general, seasonal thermal efficiencies replicated most groundwater changes during the dry fall months. The seasonal thermal efficiency for different wells ranged from ~0.8 to 2.2. The central areas with thicker evaporite crust had lower values, and the salt crust edge wells had higher values. Each well's diurnal and seasonal thermal efficiencies do not appear to be correlated.

Apparent specific yield of near-surface porous material

The specific yield is defined as the gravity-drainable pores within a sediment. The specific yield is often assumed to be constant within wells. However, this simplification does not apply to shallow wells and short periods because the drainage rate may take several days to years, and the water content of the capillary fringe and vadose zone, and antecedent conditions can vary greatly and influence measurements (Crosbie et al., 2019). Because of this, the apparent specific yield (S_{ya}) is often reported. This value factors in the effect of the capillary fringe, and it begins to approach zero as the groundwater level approaches the surface. Only at deeper groundwater depths does S_{ya} approach a sediment's specific yield (Crosbie et al., 2005; Duke, 1972).

Specific yield is highly dependent on environmental conditions and sediment texture (Healy & Cook, 2002). As Healy and Cook (2002) note, the value of Sy to use for a study can be unclear. Because of the low topography at BSF and its well-constrained precipitation and evaporative fluxes, the apparent specific yield of the shallow crust at BSF was estimated using a form of the water budget equation which relies on water table fluctuations (Gerla, 1992; Lv et al., 2021; Walton, 1970) (equation S3-5).

$$S_{ya} = \frac{\mathrm{PPT}+\mathrm{Q}_{on}-\mathrm{Q}_{off}-\mathrm{ET}-\Delta\mathrm{S}^{sw}\mathrm{sw}-\Delta\mathrm{S}^{uw}}{\frac{\Delta wd}{\Delta t}} \qquad \text{(S3-5)}$$

where PPT is precipitation, Q_{on} and Q_{off} are surface and subsurface water flow in and out of the area of interest, ET is evapotranspiration, ΔS^{sw} is surface water storage, ΔS^{uw} is unsaturated zone water storage, Δwd is the change in groundwater height, and Δt is the study period. Q_{on}, $Q_{off,}$ ΔS^{sw}, and ΔS^{uw} were assumed to be negligible because of the study site's low topography and hydraulic gradients and its near-surface water table with a capillary fringe can intersect the surface. Only dry periods with no surface water at the beginning of the interval were used. This equation then simplifies to:

$$S_{ya} = ((\mathrm{PPT} - \mathrm{E}_e)/\Delta wd)dt \qquad \text{(S3-6)}$$

where over a period dt the change in groundwater height (Δwd) is attributable to the net recharge (PPT – E_e). More simply, this is the ratio of infiltrated precipitation to the change in the water table. This calculation assumes that recharge is the only variable influencing water level. To address this concern, only daily averages of water levels that were corrected for barometric efficiency were *considered were considered to partially eliminate the influence of temperature and air pressure fluctuations upon water levels.*

The daily average value of water level, reported as the equivalent height of saturated water column and corrected for barometric efficiency (for the 3.5 m well), was used to compensate for these variables. Furthermore, the input periods to calculate S_{ya} were selected to meet the following criteria **1)** *initial water depth greater than 6 cm,* **2)** *recharge $(PPT-E_e)/E_e > 0.5$, and* **3)** *the final water depth was below the surface and did not decline rapidly in the days after precipitation (which would be indicative the reverse Wieringermeer or Lisse effects, where trapped air increases the apparent water column (Gillham, 1984; Heliotis & DeWitt, 1987)). Furthermore, to reduce to impact of the Lisse effect, apparent specific yield values less than 0.03 were not considered.*

If these conditions were met more frequently, a threshold value of >5mm of precipitation would also be included for determining S_{ya} criteria. The study intervals used here extended one day before precipitation to at least one day following precipitation. Some periods include several precipitation events.

The S_{ya} values determined by this method varied (mean of 0.09 with a standard deviation of 0.04).

Apparent specific yield relative to prior BSF research

The porosity and characteristics of evaporite crust at BSF have been previously described and indicate that the apparent specific yield reported here is reasonable. The porosity of upper halite crust samples from X-ray computed tomography measurements was determined to be 29% (±5%) (Bernau & Bowen, 2021). Porosity was also estimated from the dry density of crystalline crust from 30 samples reported by Mason & Kipp (1998). Assuming an 80-20 ratio of halite to gypsum in these samples yields an average estimated porosity of 23%. Using other proportions of halite to gypsum leads to a range of estimated porosities of 19 to 40%. Halite-rich portions of the lower part of the evaporite crust have an estimated porosity of 35-45% (Bernau & Bowen, 2021). The porosity of fine to medium sand in gypsum layers is likely between 20-50% (Bowen et al., 2018). Past examination of the fine-grained lacustrine sediments at BSF suggests a porosity of 50% and a specific yield of 10% (Turk et al., 1973).

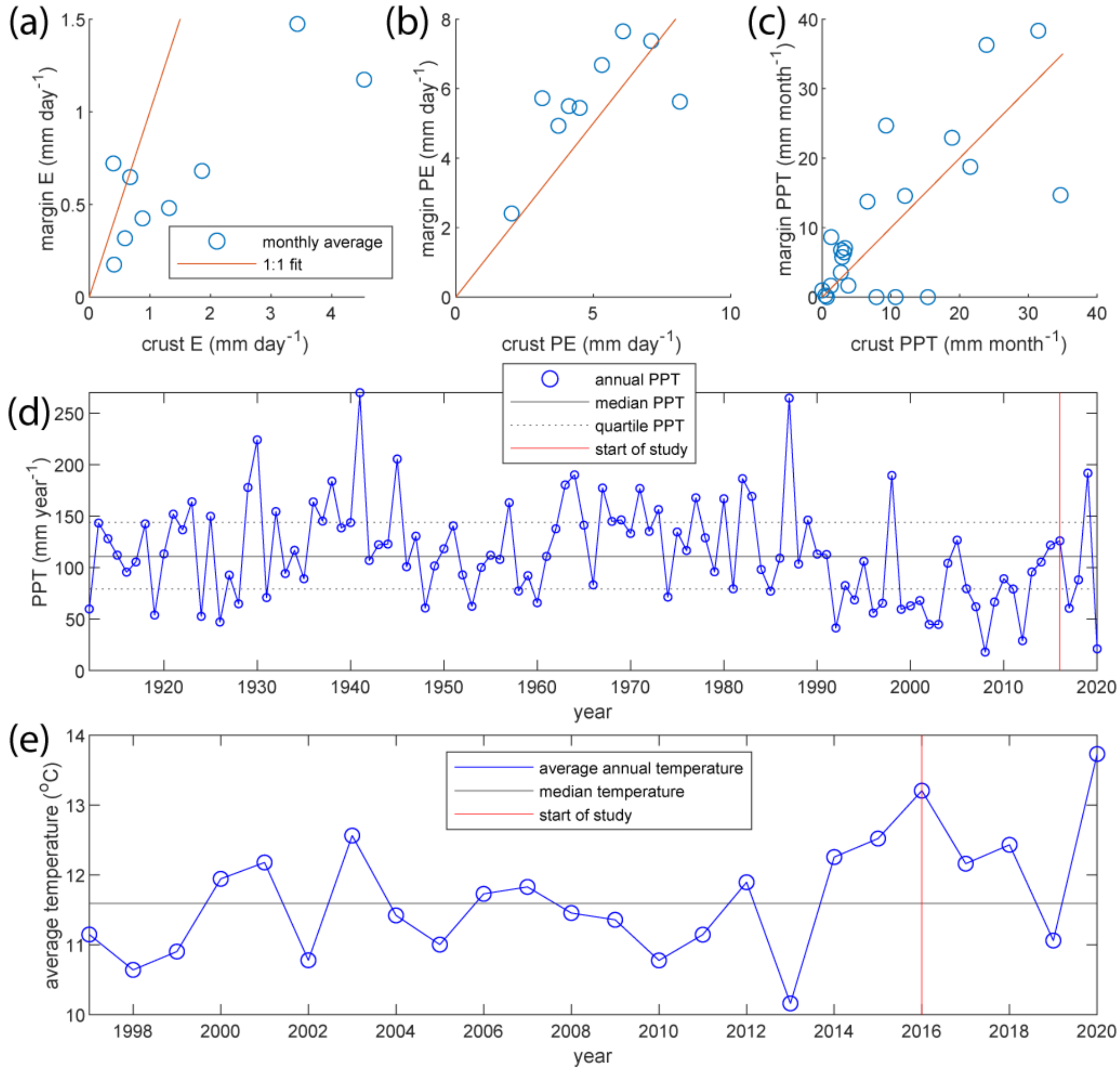

Figure S1. *Long-term climate measurements from Wendover, Utah, and comparisons of monthly average values of evaporation and potential evaporation, and monthly sums of precipitation at the western margin (margin) and center (crust) of the Bonneville Salt Flats from April to October 1993 and April to August 1994. (a) Crust evaporation (E) was higher than playa margin evaporation. (b) Potential evaporation (PE) was higher at the playa margin. (c) Cumulative precipitation (PPT) between the crust and the margin was within 5% of each other from October 1992 to July 1994. (d) Wendover, Utah, annual precipitation record demonstrates that the study period was drier than average but included unusually wet and dry years and that there has been a long-term decline in precipitation. (e) Average annual temperatures from Wendover, Utah, reveal that the study period was warmer than average. (Figure data from Mason & Kipp, 1998; NOAA Climate Data Online Portal and MesoWest).*

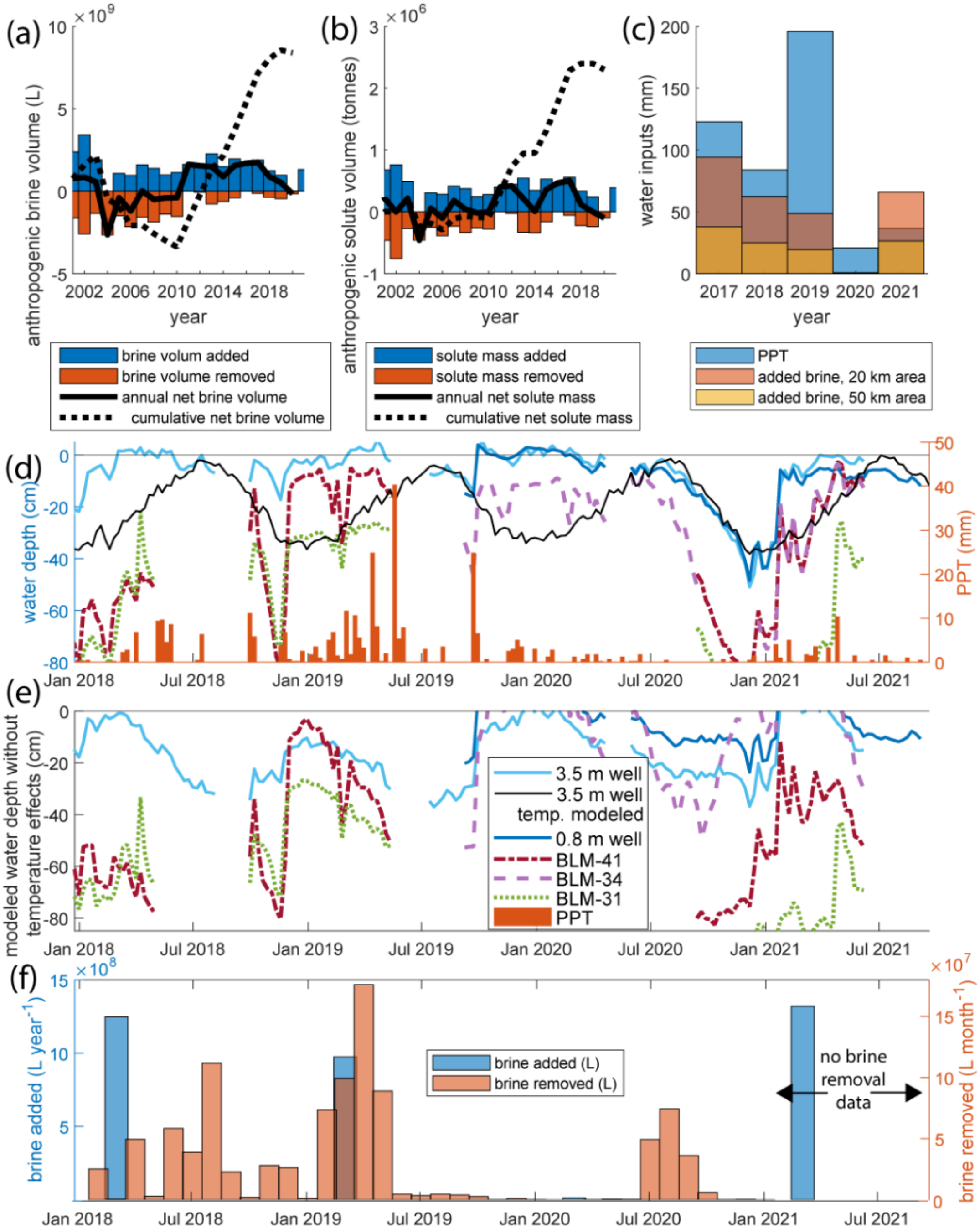

Figure S2. *Anthropogenic brine volumes and solute mass balances over time in comparison to precipitation and limited groundwater level measurements. (a) Net annual BSF anthropogenic brine volumes since 2001. (b) Mass of anthropogenic solutes added and removed from BSF (updated from Kipnis & Bowen, 2018). (c) Millimeters of water added to southwestern area of BSF annually, assuming added brine covers an area between 20 and 50 km2 (as suggested by Bowen et al., 2017). (d) Density-corrected changes in groundwater level over time (key in (e)). Wells BLM-41, BLM-34, and BLM-31 are located near brine extraction ditch. The black line shows temperature-controlled water levels in the 3.5 m well if no water inputs or output is assumed. (e) Modeled groundwater changes over with temperature effects on water levels removed. (f) Monthly values of brine addition and removal during study period.*

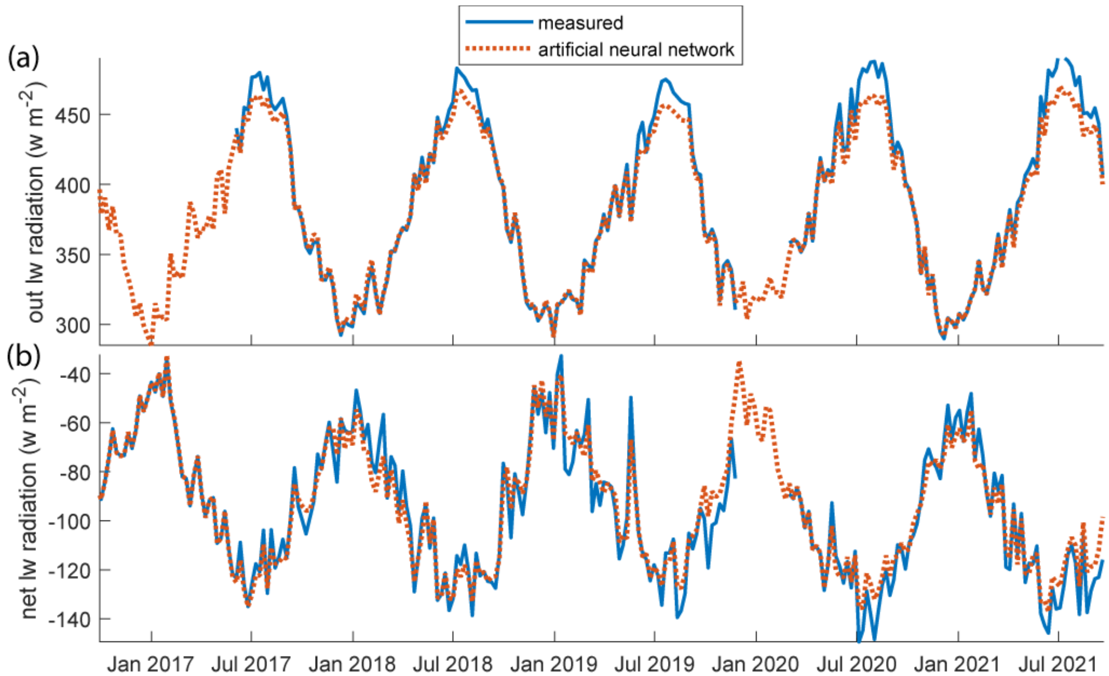

Figure S3. *Weekly average values of (a)outgoing longwave (lw) radiation and of (b) net lw radiation.*

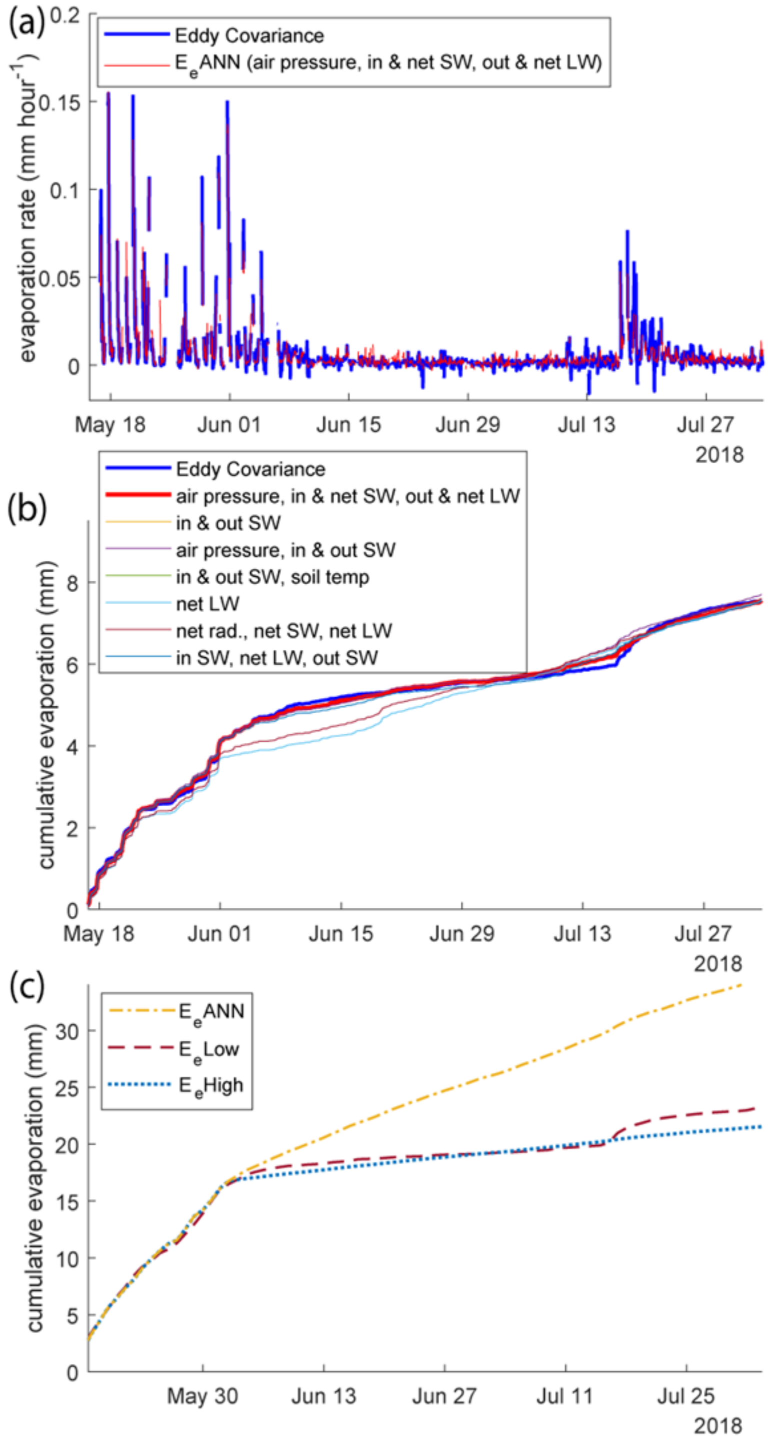

Figure S4. *Eddy-covariance evaporation values used for training compared with artificial neural network evaporation values (model inputs in addition to air temp, relative humidity, wind speed, and time of day denoted in legends with LW and SW referring to radiation). (a) Hourly evaporation rates from eddy-covariance measurements and the artificial neural network. (b) Comparison of cumulative evaporation measurements between eddy-covariance data and different artificial neural networks. (c) Calibration period cumulative values of estimated daily evaporation made with different methods. (b) and (c) period totals differ because of data gaps in (b).*

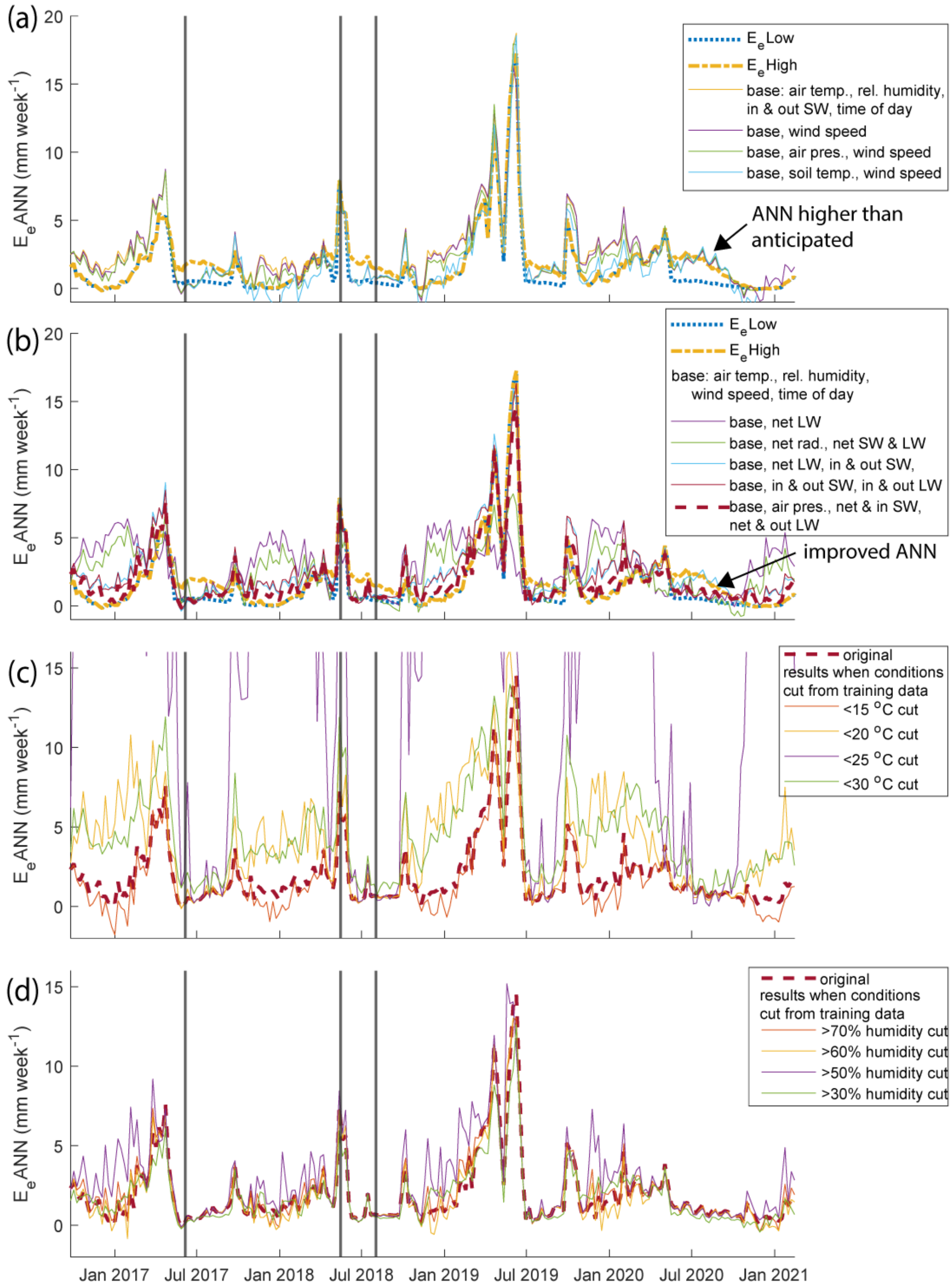

Figure S5. *Comparison of the median values of evaporation modeled with select artificial neural networks. (a-b) Estimated evaporation trained with different inputs (base inputs are described in key, with additional inputs noted). Estimated evaporation made with albedo-calibrated Penman evaporation models shown for comparison. A smaller number of inputs without longwave radiation are used in (a), while longwave radiation values are used in (b). (c-d) The impact of removing incrementally lower humidity and higher temperature periods from the training dataset on artificial neural network evaporation estimates. (c) Winter evaporation estimates were much higher when lower temperatures are removed from the training dataset. (d) Removing high humidity values from the training dataset had minimal effects on evaporation estimates.*

Figure S6. *Groundwater equivalent head correction. (a) Measured (filled circles) and calculated (lines) groundwater densities in 0.8 and 3.5 m deep wells. (b) Comparison of measured water depth and halite-saturated water equivalent head from 0.8 and 3.5-m wells. (c) The difference between head calculated with a constant density and head calculated with a variable density is between 0.5 and 1.2 cm. (d) Centimeters of difference in head between the 3.5 and 0.8-m deep wells show vertical flow gradients vary seasonally.*

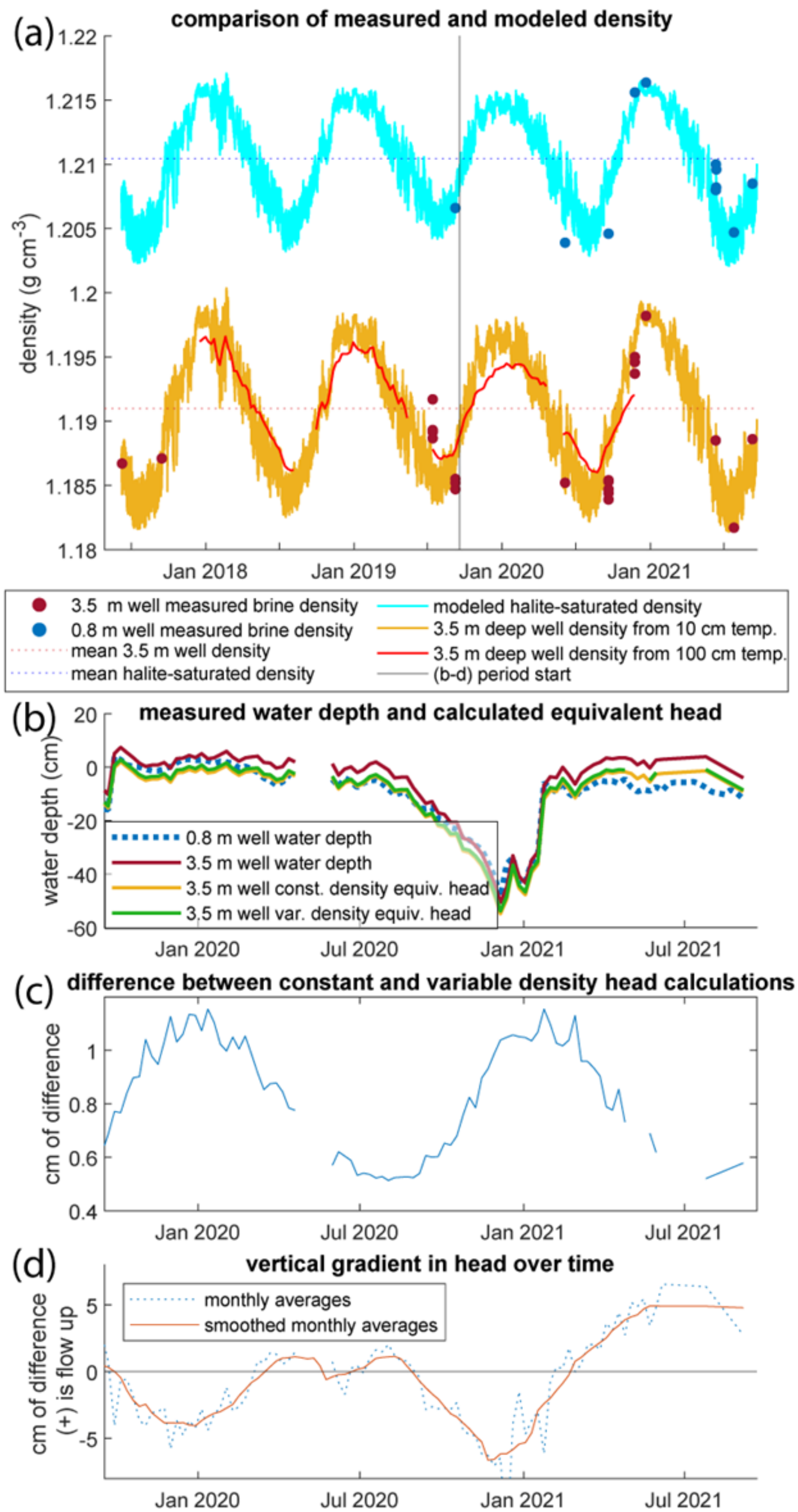

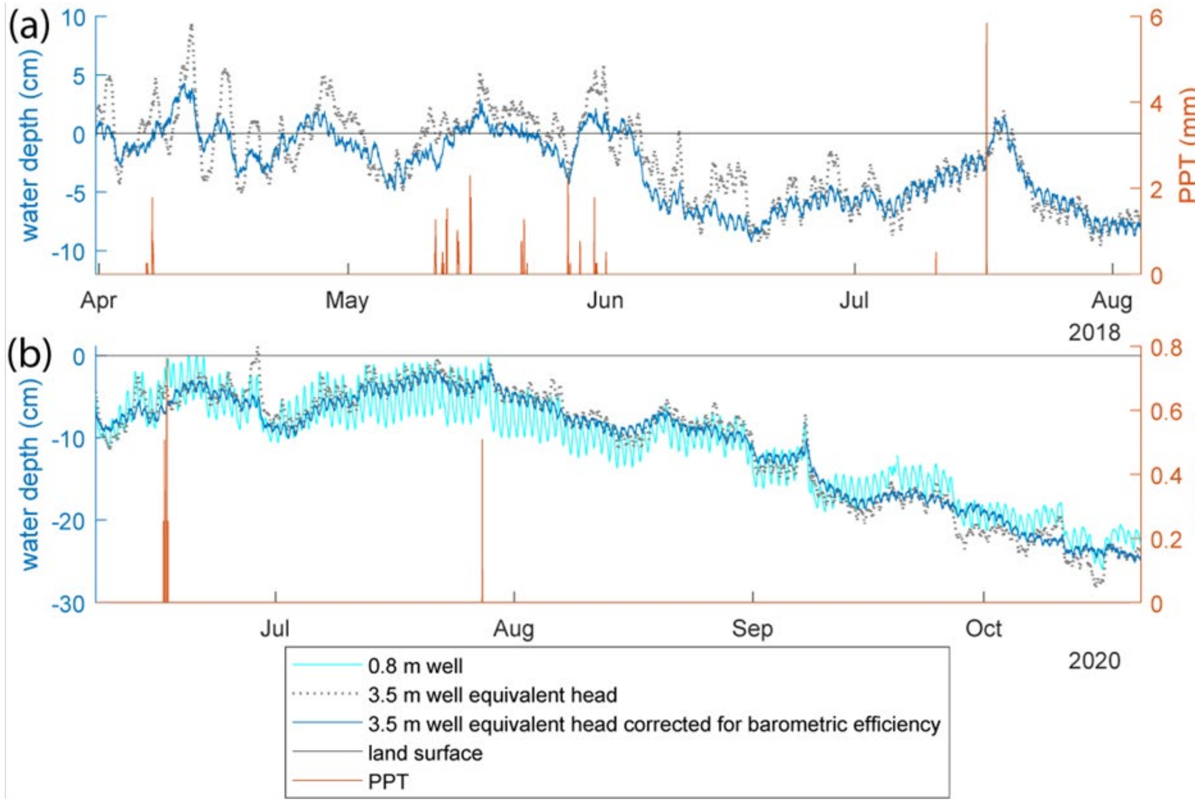

Figure S7. *Equivalent halite-saturated head and equivalent halite-saturated head corrected for barometric efficiency in the 3.5 m well. Precipitation shown for reference. (a) Barometric correction removes significant variability from the water level, making it more representative of the water table in the halite crust. (b) Comparison of corrected values and measured water table level in shallow surface (0.8 m well) demonstrates agreement between barometric-corrected head and observed near-water table water level values.*

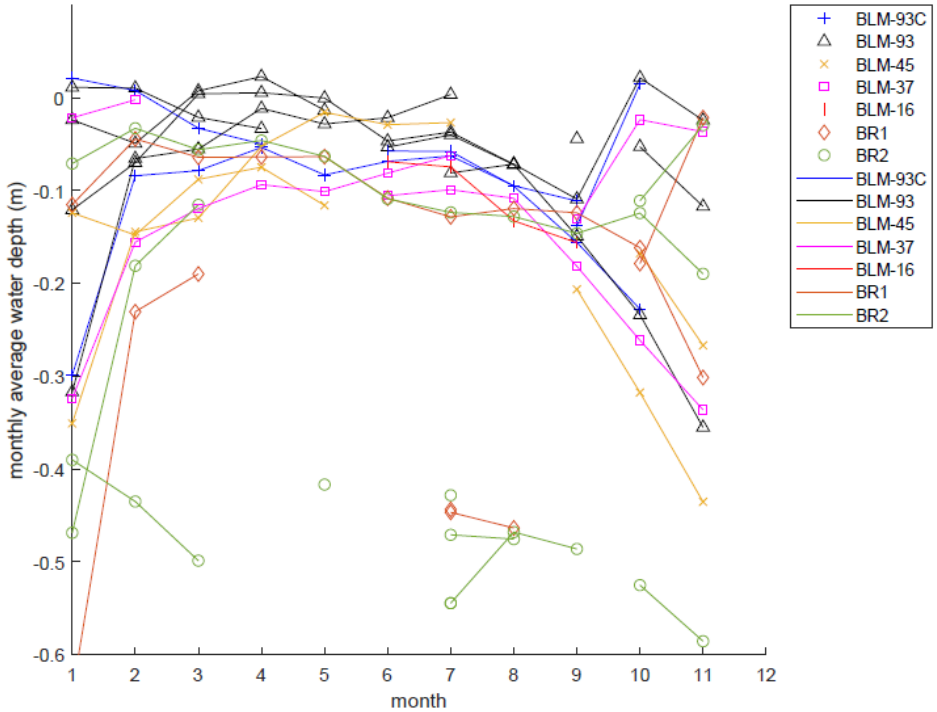

Figure S8. *Average monthly groundwater depths (corrected to equivalent head of halite-saturated brine) from wells along the centerline of the Bonneville Salt Flats, where the water table is consistently high (Lines, 1979; Mason & Kipp, 1998; Turk, 1973; and USGS water data portal). (BLM-93 and BLM-93C are the same wells as the 3.5 and 0.8 m well described in this paper). These measurements illustrate that water levels stabilizes in July to August. Other months of the year are more variable. The lower summer of 1967 water levels in BR1 and BR2 (Turk, 1973), are from when the Salduro Loop water collection ditch was active. Groundwater collection rates from this time are unknown.*

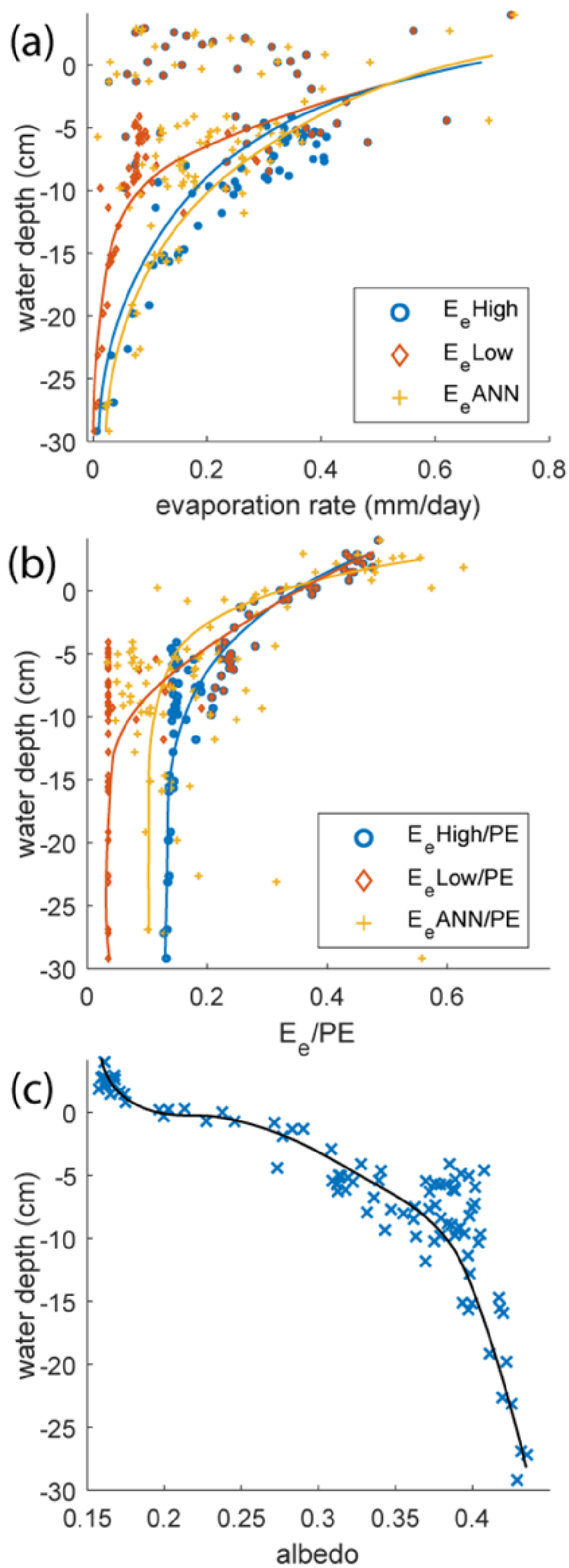

Figure S9. *Relationship between water depth in the 0.8 m well and (a) evaporation rate, (b) evaporation relative to potential evaporation, and (c) albedo.*